Radar and photometric observations and shape modeling of contact binary near-Earth Asteroid (8567) 1996 HW1

Christopher Magri [a,*], Ellen S. Howell [b], Michael C. Nolan [b], Patrick A. Taylor [b], Yanga R. Fernández [c], Michael Mueller [d], Ronald J. Vervack Jr. [e], Lance A.M. Benner [f], Jon D. Giorgini [f], Steven J. Ostro [f], Daniel J. Scheeres [g], Michael D. Hicks [f], Heath Rhoades [f], James M. Somers [h], Ninel M. Gaftonyuk [i], Vladimir V. Kouprianov [j], Yurij N. Krugly [k], Igor E. Molotov [l], Michael W. Busch [m], Jean-Luc Margot [m], Vladimir Benishek [n], Vojislava Protitch-Benishek [n], Adrian Galád [o,p], David Higgins [q], Peter Kušnirák [p], Donald P. Pray [r]

[a] University of Maine at Farmington, 173 High Street – Preble Hall, Farmington, ME 04938, USA
[b] Arecibo Observatory, HC3 Box 53995, Arecibo, PR 00612, USA
[c] University of Central Florida, Dept. of Physics, 4000 Central Florida Blvd., Orlando, FL 32828, USA
[d] Université de Nice Sophia Antipolis, CNRS, Observatoire de la Côte d'Azur, BP 4229, 06304 Nice Cedex 4, France
[e] JHU/Applied Physics Laboratory, 11100 Johns Hopkins Road, Laurel, MD 20723-6099, USA
[f] Jet Propulsion Laboratory, California Institute of Technology, Pasadena, CA 91109, USA
[g] Department of Aerospace Engineering Sciences, University of Colorado at Boulder, 429 UCB, Boulder, CO 80309-0429, USA
[h] Moorpark College, 7075 Campus Rd, Moorpark, CA 93021, USA
[i] Crimean Astrophysical Observatory, Simeiz Department, Crimea 98680, Ukraine
[j] Pulkovo Observatory of the Russian Academy of Sciences, Pulkovskoje Ave. 65-1, 196140 St. Petersburg, Russia
[k] Institute of Astronomy of Kharkiv National University, Sumska Str. 35, Kharkiv 61022, Ukraine
[l] Keldysh Institute of Applied Mathematics, RAS, Miusskaya Sq. 4, Moscow 125047, Russia
[m] Department of Earth and Space Sciences, University of California, Los Angeles, 595 Charles Young Drive East, Los Angeles, CA 90095, USA
[n] Belgrade Astronomical Observatory, Volgina 7, 11060 Belgrade 38, Serbia
[o] Modra Observatory, Department of Astronomy, Physics of the Earth, and Meteorology, FMFI UK, Bratislava SK-84248, Slovakia
[p] Astronomical Institute, Academy of Sciences of the Czech Republic, Fričova 1, CZ-25165 Ondřejov, Czech Republic
[q] Hunters Hill Observatory, 7 Malawan Street, Canberra, Australia
[r] Carbuncle Hill Observatory, P.O. Box 946, Coventry, RI 02816, USA

ARTICLE INFO

ABSTRACT

We observed near-Earth Asteroid (8567) 1996 HW1 at the Arecibo Observatory on six dates in September 2008, obtaining radar images and spectra. By combining these data with an extensive set of new lightcurves taken during 2008–2009 and with previously published lightcurves from 2005, we were able to reconstruct the object's shape and spin state. 1996 HW1 is an elongated, bifurcated object with maximum diameters of $3.8 \times 1.6 \times 1.5$ km and a contact-binary shape. It is the most bifurcated near-Earth asteroid yet studied and one of the most elongated as well. The sidereal rotation period is 8.76243 ± 0.00004 h and the pole direction is within $5°$ of ecliptic longitude and latitude $(281°, -31°)$. Radar astrometry has reduced the orbital element uncertainties by 27% relative to the *a priori* orbit solution that was based on a half-century of optical data. Simple dynamical arguments are used to demonstrate that this asteroid could have originated as a binary system that tidally decayed and merged.

1. Introduction

Asteroid (8567) 1996 HW1 – hereafter referred to as HW1 – was discovered on 23 April 1996 by T. Gehrels as part of the Spacewatch survey at Steward Observatory. HW1 is in the Amor class of near-Earth asteroids (NEAs) with a semimajor axis $a = 2.046$ AU and perihelion distance $q = 1.128$ AU.

This NEA was observed during two subsequent apparitions. Lightcurves were obtained at several observatories during June–July 2005 with the results summarized by Higgins et al. (2006) and Krugly et al. (2007). The double-peaked lightcurve exhibited a rotation period of 8.757 h and an amplitude estimated as 0.25 mag (Higgins et al.) and 0.4 mag (Krugly et al.). During the next close approach, lightcurve measurements in August 2008 (Beni-

* Corresponding author. Fax: +1 207 778 7365.
E-mail address: magri@maine.edu (C. Magri).

shek and Protitch-Benishek, 2009) gave a similar period but an amplitude of 0.82 mag, suggesting a significantly elongated body viewed much closer to its equator than in 2005. Several of us (Hicks, Rhoades, Somers) repeatedly observed the target from July 2008 through January 2009, inverting these lightcurve data using the method of Kaasalainen and Torppa (2001) and Kaasalainen et al. (2001) to estimate the spin vector and produce a convex-definite shape model that is indeed highly elongated (see animation at http://tmoa.jpl.nasa.gov/hw1.htm).

We observed the visible and IR spectrum of HW1 as part of an ongoing study of the composition and thermal properties of radar-observed NEAs. We obtained the spectrum between 0.8–2.5 μm and 1.9–4.0 μm on 19 August, 1 September, and 1 October 2008 at the NASA IRTF using the SpeX instrument (Rayner et al., 2003). R. Binzel and collaborators also obtained a spectrum on 2 September 2008 covering 0.8–2.5 μm, and this spectrum agrees well with the others. The detailed analysis of these data is reported in a companion paper (Howell et al., in preparation) and is briefly summarized here. The reflectance spectra show absorption features near 1 and 2 μm due to pyroxene. The additional band centered near 1.2 μm due to olivine is also present. HW1's visible spectrum was obtained at Palomar by one of us (Hicks), together with K. Lawrence, on 31 July and 30 September 2008. The Bus-De-Meo taxonomic class is Sq based upon these spectra (Bus and Binzel, 2002; DeMeo et al., 2009). Birlan et al. (2009) also find that HW1 is a member of the S complex in the Bus-DeMeo taxonomy, basing their classification solely on the 0.8–2.5 μm spectrum. The thermal emission in the spectrum beyond 2.8 μm is best fit with a visible albedo of about 0.3. The H magnitude is 15.3, which together with our albedo estimate suggests a diameter of 2.1 km, assuming a spherical shape (Pravec and Harris, 2007).

On 12 September 2008 HW1 passed just 0.135 AU from Earth. We took advantage of this close approach to observe the asteroid with radar, obtaining images and echo power spectra that we then used, together with lightcurves, to carry out a 3D shape/spin reconstruction. The most striking result of this modeling effort is that HW1 is far from being a quasi-convex object and has, in fact, one of the most bifurcated contact-binary shapes seen to date in the near-Earth population.

The next section describes our observations, while Section 3 summarizes the shape/spin reconstruction procedure. Section 4 presents our model of HW1. We discuss our results in Section 5.

2. Observations and data reduction

2.1. Radar data

The continuous-wave (CW, Doppler-only) spectra and delay-Doppler images discussed here were obtained on six dates during 15–21 September 2008 (see Table 1) at the Arecibo Observatory. Our observing procedure and data reduction methods are fully described by Magri et al. (2007) and we only summarize them here. For each transmit–receive cycle ("run") we transmitted a circularly polarized signal at 2380 MHz for a duration equal to the round-trip light time (roughly 2.3 min). For CW runs the transmitted signal was monochromatic, while for imaging runs a repeating pseudo-random binary code was used to modulate (flip or not flip) the sinusoid's phase once every 0.50 μs (the "baud length"). We then switched to receive mode for a duration equal to the round-trip light time, receiving power in both the circular polarization sense opposite that transmitted (OC) and in the same sense (SC) and sampling the echo at a rate of one complex voltage sample per baud. Single reflections from a smooth surface produce a purely OC echo, whereas multiple reflections, and/or diffuse scattering from wavelength-scale structure (e.g., subsurface voids) within a meter or so of the surface, yield an echo with nonzero SC/OC circular polarization ratio.

Images were decoded by cross-correlating the voltage time series with the transmitted code, thus providing time delay resolution. Because delay is proportional to distance from Earth (range), it follows that images spatially resolve the target along the line of sight. Then the decoded signal in each delay cell was Fourier transformed in order to provide Doppler resolution; the same was done for each CW spectrum. Doppler resolution is important because the target's rotation spreads the echo's frequency about the transmit frequency; this gives us information about surface elements' radial velocities, information that places a joint constraint on the target's shape and spin vector. Images resolve the target in both delay (range) and Doppler; CW spectra provide only Doppler resolution but generally have higher signal-to-noise ratio (SNR) than images, thus making them particularly useful for determining the target's radar cross section and reflectivity.

The result of these observations and reductions was 119 delay-Doppler images with 0.238 Hz × 0.50 μs pixels, plus 16 CW spectra with 0.20-Hz resolution. In order to improve SNR for an initial look

Table 1
Radar observations.

Observing date (UT)	Type	Runs	Receive start–end (UT)	RA (°)	Dec (°)	Dist (AU)	δ_{rad} (°)	Rot. phase (°)	Orbital solution	Code	Baud (μs)	Δf (Hz)	Power (kW)	N_{looks}
15 September 2008	CW	5	04:50:15–05:10:35	18	+9	0.135	+9	234–248	170	–	–	0.200	561	24
	Delay-Doppler	25	05:20:18–07:12:06	18	+9	0.135	+9	255–332	170	65,535	0.50	0.238	604	30
16 September 2008	CW	3	05:18:02–05:29:16	19	+9	0.136	+9	161–169	170	–	–	0.200	589	24
	Delay-Doppler	21	05:39:17–07:12:05	19	+9	0.136	+9	176–239	170	8191	0.50	0.238	589	30
17 September 2008	CW	3	05:01:19–05:12:38	20	+8	0.136	+9	57–65	170	–	–	0.200	608	24
	Delay-Doppler	21	05:21:39–07:09:32	21	+8	0.137	+9	71–145	170	8191	0.50	0.238	608	30
18 September 2008	CW	2	05:08:26–05:15:10	22	+7	0.137	+9	329–334	172	–	–	0.200	606	24
	Delay-Doppler	19	05:22:27–06:46:48	22	+7	0.137	+9	339–37	172	8191	0.50	0.238	623	30
19 September 2008	CW	2	05:03:29–05:10:16	23	+6	0.138	+9	234–238	174	–	–	0.200	595	24
	Delay-Doppler	25	05:18:01–07:10:35	23	+6	0.138	+9	244–320	174	8191	0.50	0.238	595	31
21 September 2008	CW	1	05:10:39–05:12:51	25	+5	0.140	+9	53–55	174	–	–	0.200	614	24
	Delay-Doppler	8	05:19:17–05:54:09	25	+5	0.140	+9	59–83	174	8191	0.50	0.238	614	31

Notes: All experiments involved transmission at 2380 MHz and reception in both OC and SC polarizations. On each line we give the observing date; the type of observation; the number of transmit–receive cycles, or runs; the starting and ending receive times; right ascension, declination, and distance from Earth; subradar latitude δ_{rad} at mid-receive; the range of rotation phase covered (with zero phase occurring at 05:53:04 UT on 18 September 2008); the orbital solution used for our delay-Doppler ephemeris predictions; the length of the repeating binary phase code; the baud length; the raw frequency resolution Δf of our reduced data; the transmitted power; and the number of independent estimates of the power distribution, or "looks," that were incoherently summed to produce the spectrum or image for each run. Data were taken at a rate of one sample per baud for all delay-Doppler imaging runs. Rotation phase is defined as 360° minus subradar east longitude, with 0° and 180° corresponding to maximally end-on views according to the radar-and-lightcurve-based shape/spin model presented in Section 4. Plane-of-sky motion was taken into account when computing rotation phase.
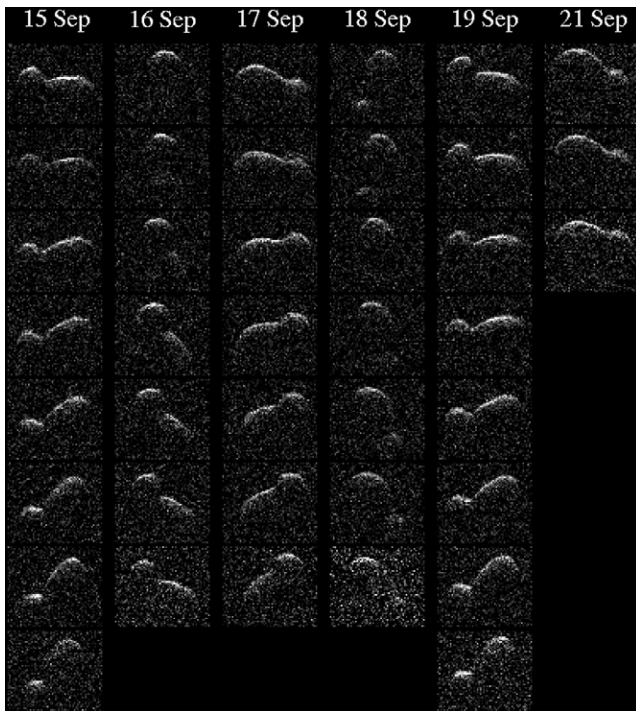
Fig. 1. Delay-Doppler images of HW1. OC images obtained on each of the six indicated 2008 observing dates are displayed, arranged chronologically from top to bottom. Each displayed image is the sum of three consecutive runs listed in Table 1, except for the third 21 September image which is the sum of only two runs. (The final sums for 15 and 19 September have been omitted from the figure.) Images are oriented with Earth toward the top and positive Doppler to the right. Each pixel is 0.238 Hz × 0.50 μs, corresponding to 0.076 km × 0.075 km at our mean subradar latitude of +9°; each image spans 14.3 Hz × 25.5 μs, corresponding to 4.57 km × 3.82 km. All images are on the same grayscale in radar cross section. The asteroid rotated through about 9° during the time (~14 min) spanned by each set of three runs; the resulting smearing can be seen in the second 17 September sum. Individual runs, each one covering only 3° of rotation, were used as input to shape modeling and are shown as the "obs" images in Fig. 7.

at our data, we summed sets of three images (Fig. 1) and smoothed each spectrum (Fig. 2). We discuss these summed/smoothed data below. In order to minimize rotational smearing (~3° per run) we used the individual images for shape modeling; similarly, we used unsmoothed spectra to ensure that we were not smoothing away genuine features in the data. Because the SC echo from HW1 was several times weaker than the OC echo, only OC images and spectra were used for shape reconstruction. The data are calibrated, so that we can treat them as absolute "photometry"; for Arecibo observations the typical absolute calibration uncertainty is ~25% and night-to-night variations are ~10%.

Our images and spectra clearly show an elongated, bilobate asteroid. CW bandwidths varied between about 8 Hz and 12 Hz from day to day (Fig. 2), implying that HW1's pole-on silhouette is elongated by a factor of at least 1.5. (Because we did not obtain an end-on view in CW (Table 1) the elongation is biased downward by some amount that depends on the details of the shape.) The wider spectra also have significant dips, suggesting a bifurcated target that presents less projected area to the radar at a particular projected distance from the spin axis (proportional to the Doppler frequency of the dip). The images cover a larger range of rotation phases (Fig. 1, Table 1), so their bandwidths range from 12 Hz down to as little as 5 Hz. These bandwidths, combined with our *a priori* constraints on HW1's spin vector (see Introduction), suggest equatorial diameters of about 3.8 × 1.6 km. The signal in the wider images also exhibits a "valley" – a region of increased delay values (distances from Earth) relative to adjacent portions of the echo's

leading edge – that is the unmistakable signature of a deep surface concavity that faces the radar. Such concavities are seen on opposite sides of the asteroid (e.g., the third images displayed for 15 and 17 September in Fig. 1), indicating a two-lobed object; the fact that the concavities are off-center in Doppler implies that the lobes' longest diameters are in a roughly 2:1 ratio. The narrower images confirm this picture of HW1. The signal extends much deeper in delay than for the widest images, as expected for a more end-on view of an elongated object. This signal often becomes particularly strong at large distances from the observer (e.g., the bottom-left image in Fig. 1) owing to scattering from the Earth-facing side of the more distant of the two lobes, whereas the echo from a convex target would gradually weaken with distance.

2.2. Lightcurve data

For the shape reconstruction described in Section 3.2 we used, in addition to the radar data, all the lightcurve data from the analyses of Higgins et al. (2006), Krugly et al. (2007), and Benishek and Protitch-Benishek (2009). (Some of the Higgins et al. data from Modra Observatory and Ondřejov Observatory have been edited or rereduced for the present work.) We also included lightcurves obtained at Kharkiv Observatory and Simeiz Observatory in 2008; the CCD observations and data processing for these measurements followed standard procedures that were described in detail by Krugly et al. (2002). Finally, we used lightcurves taken at Table Mountain Observatory in 2008–2009. In all we used 63 lightcurves, which are summarized in Table 2. Although some of the photometry was absolute photometry, we treated it all as relative photometry, to avoid difficulties in combining datasets taken at different observatories under different observing conditions and viewing geometries. We treated each night separately for shape reconstruction rather than "linking" lightcurves from successive nights. The visible reflectance of HW1 was modeled using a linear combination of Lommel-Seeliger and Lambert scattering (Kaasalainen et al., 2001).

3. Shape modeling

3.1. Lightcurve-based convex model

Using lightcurves obtained at Table Mountain Observatory, several of us (Hicks, Rhoades, Somers) determined a shape model and spin vector for HW1 via the method of Kaasalainen and collaborators (Kaasalainen and Torppa, 2001; Kaasalainen et al., 2001). The shape was constrained to be convex-definite and hence is a "gift-wrapped" view of the true object. This model is displayed in Fig. 3. The ratio of the long to intermediate diameter in the equatorial plane is ~1.63 and the ratio of the intermediate to short (polar) diameter is ~1.34. (The overall linear scale of the model is undetermined.) The derived pole direction is at ecliptic longitude and latitude $(\lambda, \beta) = (282°, -39°)$ and the derived sidereal rotation period is 8.7627 h. This spin vector agrees well with the result obtained by including other lightcurves and radar data (Section 3.2.2).

3.2. Radar-and-lightcurve-based model

Modeling the shape and spin state of HW1 provided new challenges for us, so this section gives an overview of the lengthy process that was required. First we explain how we created a two-lobed initial model and how we effectively vignetted our radar images so as to minimize the detrimental effects of noise. Then we outline how we estimated the asteroid's pole direction, and fi-
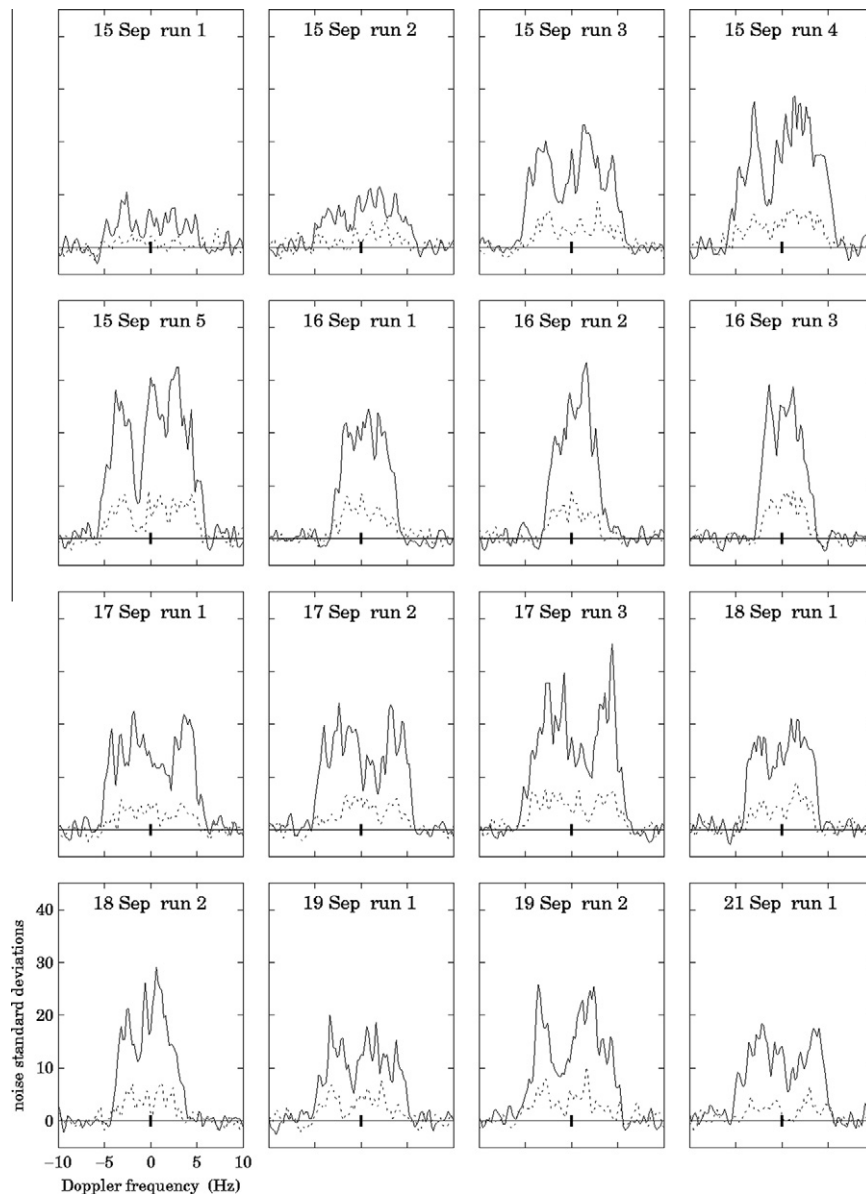
Fig. 2. OC (solid lines) and SC (dashed lines) CW echo spectra obtained for HW1. Echo power, in units of standard deviations of the noise, is plotted vs. Doppler frequency (Hz) relative to that of hypothetical echoes from the target's center of mass. All plots have identical axis scales, shown on the plot at lower left. The vertical bar at the origin indicates ±1 standard deviation of the OC noise. Each label gives the 2008 observing date and the CW run number on that date. For clarity all spectra have been smoothed from the raw frequency resolution of 0.20 Hz to an effective resolution of 0.50 Hz. Unsmoothed OC spectra were used as input to shape modeling and are shown in Fig. 8.

nally we describe the "vertex" fits in which the model's detailed shape was determined.

3.2.1. Initial model

The images in Fig. 1 clearly imply that HW1 has deep concavities at scales comparable to its radius. Thus our usual approach of fitting a triaxial ellipsoid as our initial model would have produced unrealistic results. In fact, our attempts to fit the shape as an eighth-degree spherical harmonic expansion also failed, producing numerous lobes as spurious mathematical artifacts.

We thus initialized our model as a set of *three* intersecting ellipsoids, one representing a large lobe and two smaller ones combining to form a smaller second lobe. We used three rather than two ellipsoids so that the smaller lobe could be asymmetric, in keeping with the fact that this lobe's radar echoes for 15 and 17 September – obtained about 180° apart in rotation phase – are not exact mirror images of each other (Fig. 1). Each of the three ellipsoids was

described by nine parameters that govern its shape, its displacement relative to the model's overall center of mass (COM), and its orientation. However, the presence of so many parameters in a crude initial model exacerbated a second problem: our images are not very strong. The signal seems obvious in Fig. 1, but this is due to the pattern-recognition capabilities of the human eye–brain system. Our shape-modeling software package, SHAPE (Hudson, 1993), only sees some moderately strong pixels (4–5 standard deviations of the background noise) amidst a far larger number of noise pixels. This means that reduced χ^2 is not much greater than 1.0 even for a poor model, making it difficult for SHAPE to adjust and improve the model. Hence we needed to provide the software with human guidance to a much greater extent than for previously published radar shape models.

First we set out to create by hand an initial model that fit the images reasonably well. Normally the many-to-one nature of the delay-Doppler mapping (see Fig. 1 of Ostro et al. (2002)) necessi-

Table 2
Lightcurve observations.

Observing date (UT)	Observatory	Filter	N_{lc}	N_{pts}	RA (°)	Dec (°)	Δ (AU)	r (AU)	α (°)	δ_{lc} (°)
26–27 June 2005	Modra	rel	1	53	264	+0	0.571	1.549	17	−33
27–28 June 2005	Modra	rel	1	23	264	+0	0.566	1.543	17	−33
28–29 June 2005	Modra	rel	1	16	263	+0	0.562	1.537	18	−33
2–3 July 2005	Modra	rel	1	58	262	+1	0.547	1.513	20	−32
3 July 2005	Ondřejov	rel	1	8	262	+1	0.544	1.508	21	−32
3–4 July 2005	Modra	rel	1	51	262	+1	0.544	1.508	21	−32
4 July 2005	Hunters Hill	rel	1	43	261	+1	0.542	1.504	21	−32
5 July 2005	Carbuncle Hill	rel	1	14	261	+1	0.540	1.500	21	−32
5 July 2005	Hunters Hill	rel	1	45	261	+1	0.539	1.499	22	−32
12 July 2005	Ondřejov	rel	1	32	259	+1	0.519	1.455	26	−31
13 July 2005	Ondřejov	rel	1	14	259	+1	0.517	1.449	27	−31
25 July 2005	Simeiz	rel	1	23	256	+0	0.498	1.381	35	−31
26 July 2005	Simeiz	R	1	40	256	−1	0.497	1.376	36	−31
27 July 2005	Simeiz	R	1	33	256	−1	0.496	1.371	36	−31
2–3 June 2008	Simeiz	rel	1	34	303	−1	0.700	1.531	33	−35
3–4 June 2008	Simeiz	rel	1	34	303	−1	0.689	1.525	33	−35
4 July 2008	Table Mountain	rel	2	196	314	+9	0.418	1.351	31	−23
7 July 2008	Table Mountain	BVRI	4	74	315	+10	0.396	1.335	31	−21
12–13 July 2008	Simeiz	R	1	77	317	+12	0.358	1.306	31	−19
13 July 2008	Simeiz	rel	1	40	317	+12	0.352	1.302	31	−19
14–15 July 2008	Simeiz	rel	1	71	318	+13	0.345	1.297	31	−18
19 July 2008	Table Mountain	rel	1	32	320	+14	0.318	1.275	31	−16
26 July 2008	Table Mountain	BVRI	4	84	323	+17	0.279	1.244	31	−13
9 August 2008	Table Mountain	rel	1	44	332	+20	0.213	1.190	31	−6
11–12 August 2008	Belgrade	rel	2	131	334	+20	0.202	1.181	31	−5
12–13 August 2008	Belgrade	rel	2	198	335	+21	0.199	1.178	31	−5
13–14 August 2008	Belgrade	rel	2	151	336	+21	0.195	1.175	31	−4
14–15 August 2008	Belgrade	rel	2	229	337	+21	0.192	1.172	31	−4
15 August 2008	Table Mountain	rel	2	137	337	+21	0.190	1.171	31	−4
25 August 2008	Simeiz	rel	1	120	349	+20	0.158	1.146	29	+2
26–27 August 2008	Simeiz	VR	2	704	350	+20	0.155	1.144	29	+2
8 September 2008	Kharkiv	BVRI	4	288	9	+14	0.136	1.129	25	+7
19 September 2008	Table Mountain	R	1	327	23	+6	0.138	1.129	24	+9
21–22 October 2008	Simeiz	V	1	291	44	−10	0.225	1.200	22	+7
22–23 October 2008	Simeiz	V	1	357	44	−10	0.229	1.203	22	+7
7 November 2008	Table Mountain	R	1	229	45	−11	0.303	1.267	21	+8
15 November 2008	Table Mountain	rel	1	208	46	−10	0.350	1.306	22	+8
24 November 2008	Table Mountain	rel	1	94	46	−8	0.411	1.353	23	+10
2 December 2008	Simeiz	rel	1	64	47	−6	0.477	1.400	25	+12
5 December 2008	Table Mountain	rel	1	83	47	−6	0.498	1.414	25	+13
6 December 2008	Table Mountain	rel	1	41	47	−6	0.505	1.418	25	+13
19 December 2008	Table Mountain	rel	1	66	49	−2	0.629	1.494	28	+17
20 December 2008	Table Mountain	rel	1	59	49	−2	0.639	1.500	28	+17
30 December 2008	Table Mountain	rel	2	112	51	+1	0.748	1.560	30	+20
2 January 2009	Table Mountain	R	1	108	52	+1	0.783	1.578	30	+21
8 January 2009	Table Mountain	rel	1	64	54	+3	0.856	1.614	31	+24

Notes: On each line we give the observing date; the observatory; the photometric filter (if absolute photometry) or else "rel" for relative photometry; the number of lightcurves and number of data points; right ascension, declination, geocentric distance Δ, and heliocentric distance r; solar phase angle α; and subobserver latitude δ_{lc}.
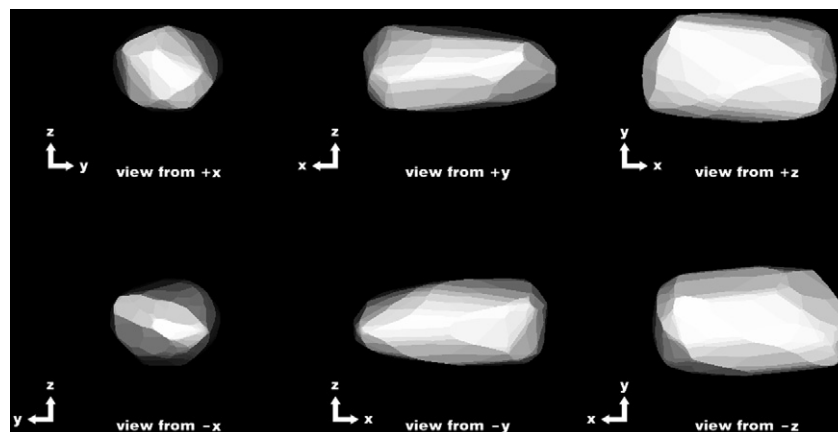

Fig. 3. Views of the lightcurve-based convex-definite HW1 model along its principal-axis directions. The overall linear scale of the model is undetermined.

tates the use of computer software to accomplish such a data inversion; this, of course, is what SHAPE is designed to do. But

most of the signal in our HW1 images is on the echo's leading edge, which is mapped one-to-one from the target's instantaneous

apparent equator to delay-Doppler space. Thus it was possible for us to generate a plausible initial model guided only by visual inspection of the images.

We started by choosing a plausible pole direction, as the light-curve-based pole estimate given in Section 3.1 was not yet available at the time. Because the lightcurve amplitude was much greater in 2008 than in 2005, and because the maximum Doppler bandwidth did not change significantly during our radar experiment, we created a list of pole positions that imply a somewhat equatorial view in August–September 2008 and a more pole-on view in June–July 2005. We then randomly adopted one of these poles for our initial model, at $(\lambda, \beta) = (270°, +45°)$. (In the following section we will see that this initial guess turned out to be very far off.) Next we used SHAPE to run the forward problem repeatedly, generating model predictions (synthetic images). After visually inspecting each set of predictions, we adjusted our model by hand, resizing and shifting and rotating each of the three ellipsoids so as to improve the match between the predictions and the actual data. The result is shown in Fig. 4.

Once we were satisfied with our initial model, we sought to "eliminate" as many noise pixels as possible so that the difference between a poor model and a good one would be more apparent to SHAPE. In order to do this we ran the forward problem again to locate the predicted power in delay-Doppler space, then used this information to create a pixel mask that told the software to ignore (set to zero) the χ^2 contributions of any image pixels that were more than five pixels away from any predicted echo power. We used this mask to run a trial fit in which SHAPE was permitted to adjust the model's shape, thus producing an improved model that was then used to generate a second, improved pixel mask, and so on for several iterations. The final mask ignored any image pixels that were more than three pixels away from any pixel whose predicted signal is greater than 10^{-6} standard deviations of the background noise. This mask was used for all fits described below.

In order to check that we were not masking out any signal from HW1, we visually inspected the masked-out regions. Additionally, we looked at the distribution of power values for the masked-out pixels in each image. For pure noise, these values should be χ^2-distributed, so we applied a Wilson–Hilferty cube-root transformation to the data (Kendall and Stuart, 1977) to turn this into an approximately Gaussian distribution. We then verified that the number of pixels more than three standard deviations away from the mean did not exceed what would be expected by chance, thus confirming that no significant echo power was being masked out.

3.2.2. Pole searches

Our next step was to model HW1's shape/spin state by having SHAPE solve the inverse problem. For each fitting run we had the program fit the 27 (=9 × 3) shape-related parameters already mentioned, plus the sidereal spin rate, the absolute rotation phase at the start of the radar experiment, the radar reflectivity at normal incidence, the relative weighting factor for Lommel-Seeliger vs. Lambert scattering in the optical regime, and several coefficients that account for imperfections in the delay-Doppler ephemeris predictions during the radar experiment. At this early stage we fixed the exponent of the radar scattering law (which determines how diffuse vs. specular the scattering is) at 2.0, corresponding to Lambert scattering. Magri et al. (2007) provides a more detailed description of these parameters and of the fitting procedure.

Our first task was to determine the pole direction, as our initial guess was merely plausible. The lightcurve data are crucial in this step, so we gave them enough weight in the fit relative to the radar data that they would initially contribute several tens of percent to χ^2, large enough to make it clear which pole directions are better than others but not so large as to overwhelm the radar data and thus tempt SHAPE to undo the hand-fitting described earlier. (The χ^2 computation occurs in intensity space rather than magnitude space.) Because we treated all lightcurve data as relative photometry and did not attempt to link lightcurves, SHAPE was permitted to shift (in magnitude space) each of the 63 synthetic lightcurves in order to obtain the best fit to the data. The program accounts for self-shadowing, which is very important given the model's bifurcated shape.

We started by running an all-sky grid search for the pole, fitting 186 models whose pole directions were spaced at 15° resolution. We sped up these modeling runs by using only 20 lightcurves, selected to provide good rotational coverage over a wide range of epochs, and by averaging the lightcurve points over rotation phase to 12° resolution. In order to maximize SHAPE's chances of correctly fitting the delay-Doppler images, we separately initialized each model's orientation so that its absolute rotation phase at the start of the radar experiment was approximately correct. Each model's pole position was held fixed. Penalty functions were applied so as to keep each model's overall COM close to the origin and its shortest principal axis of inertia close to the spin axis – that is, to enforce uniform density and principal-axis rotation. This grid search demonstrated that the pole was most likely in the vicinity of (275°, −35°) but with some chance of it being near (110°, −60°); no northern poles were plausible, even when we took the best possibilities and hand-edited the models to try to improve the fits.
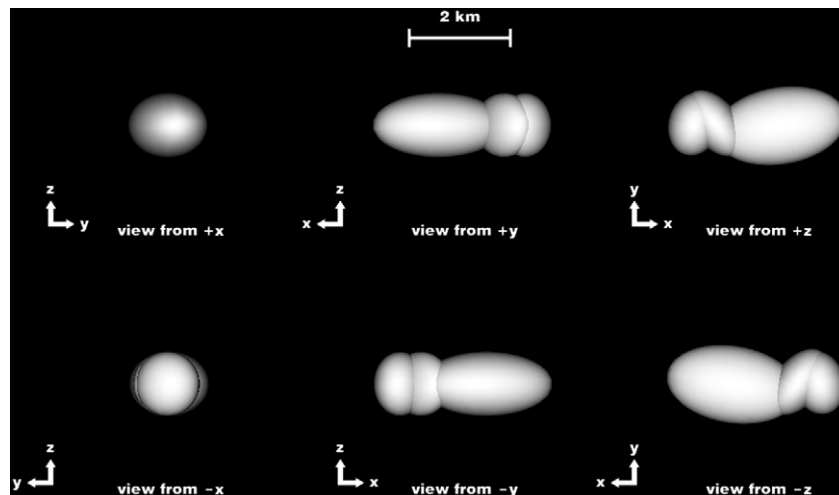

Fig. 4. Views of our initial three-ellipsoid HW1 model along its principal-axis directions.

Next we ran two new grid searches, each one covering (at 5° resolution) two circles of 30° radius centered on the two sky positions listed above. In one search, the pole position of each model was held fixed, while in the other, SHAPE was permitted to adjust the pole longitude and latitude. The latter search in particular demonstrated that the pole must be somewhere near (281°, −32°): when an initial pole direction in the vicinity of (110°, −60°) was permitted to change, it typically moved away by 10–20° and yielded a mediocre fit to the data, especially the lightcurve data. (The results of that search and of the earlier all-sky grid search are displayed in Fig. 5.) Hence for our final pole searches we covered the region near (281°, −32°) at 3° resolution, eventually using all 63 lightcurves and no longer averaging the lightcurve data over rotation phase. Here our two methods – fitting the pole direction vs. holding it fixed – produced very similar results, allowing us to estimate a pole direction within a 5° radius of (281°, −31°).

3.2.3. Vertex fits

SHAPE internally represented ("realized") our three-ellipsoid model as three intersecting polyhedral solids with triangular facets and a total of 1814 vertices, and at the end of the ellipsoid fit for our adopted pole direction, 1392 of these vertices were located on the model's exterior. We extended our code so that it could merge these ellipsoids – discarding the interior vertices and repairing the "broken" facets along the intersections between ellipsoids – to produce a one-component polyhedral "vertex" model. We ran a vertex fit on this model, adjusting each of the 1392 vertex positions individually. The pole direction was fixed at (281°, −31°), as trial vertex fits for which the pole was allowed to vary produced less than 1° of change.

At this stage we added another penalty function ("nonsmooth") that strongly suppressed small-scale topography. One reason for this is that HW1's pole direction implies a near-equatorial view throughout the radar experiment, so "north–south ambiguity" prevents us from uniquely determining topography away from the target's apparent equator (see Magri et al., 2007). An even more basic reason is that, as was mentioned earlier, our images do not display much echo power behind the leading edge: most of the signal was scattered from the apparent equator or else was lost in the noise. Thus, the fact that we have discouraged topographical complexity in our model should not be taken as a statement that none exists on HW1.

We also experimented with the "concavity" penalty function to see what the effect of suppressing small-scale concavities would be. Given the strong "nonsmooth" penalty that was already being applied, the "concavity" penalty primarily influenced the "neck" between the two lobes of our model (see Section 4.1), forcing it to be more U-shaped than V-shaped. This had little effect on the fits to the radar data but somewhat degraded the lightcurve fits, so we used a low "concavity" penalty weight for the run that produced our final model.

For some runs we used the "flattening" penalty, equal to $(b/c − 1)^4$ for $b/c > 1$ and 0 for $b/c \leqslant 1$; here b and c are the intermediate and short radii of the dynamically equivalent equal-volume ellipsoid (DEEVE), the hypothetical ellipsoid that has the same volume as our model and has principal moments of inertia in the same relative proportions as does our model. (The penalty, when used at all, was applied during both the three-ellipsoid stage and the vertex stage of the fit.) The "flattening" penalty normally hinders polar flattening, but for some runs we applied it with a negative penalty weight, thus leading SHAPE to *encourage* flattening. Laboratory "ground truth" obtained with lasers and clay models shows that radar-based shape reconstructions derived from near-equatorial data are biased toward overly large polar dimensions
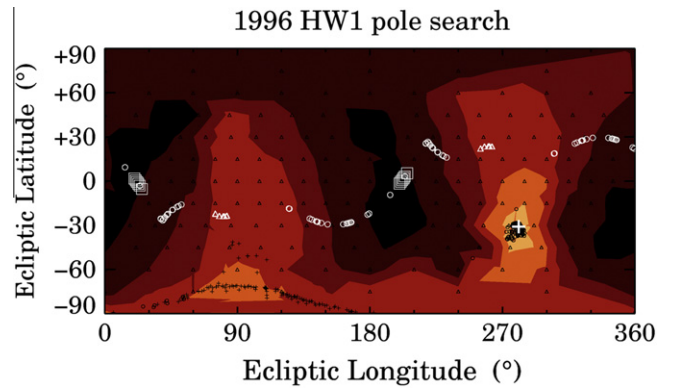

Fig. 5. Results of two grid searches for HW1's pole direction. Each small black symbol marks the final ecliptic pole coordinates for a three-ellipsoid modeling run. Bright contour levels are associated with better models that yielded lower values of reduced χ^2. The regularly spaced black triangles represent an all-sky grid search at 15° resolution, where the pole direction for each model was held constant. Other black symbols show the results of a subsequent grid search that permitted each model's pole direction to vary during the fit; the initial pole positions covered two regions on the sky, centered at ecliptic longitude and latitude $(\lambda, \beta) = (275°, −35°)$ and $(110°, −60°)$, at 5° resolution. Models whose poles started in the latter region are marked by black crosses; these models usually moved away to some pole position along the continuous curve seen at bottom left (which is actually a map-distorted view of a circle on the sky) and produced mediocre fits to the data. Models in the other region, marked by black circles, instead tended to converge toward a common pole direction and produced the lowest reduced χ^2 values, indicating that this is where HW1's pole lies. The white cross marks the best-fit pole at (281°, −31°) that we derived following a final refined set of grid searches (see text). Other white symbols mark HW1's sky position on the dates when data were obtained: large white squares denote the 2008 radar experiment, small white triangles the 2005 lightcurves, and small white circles the 2008–2009 lightcurves. The antipodal sky positions, lying in the longitude range $\lambda \sim 60°$ through 240°, have also been marked, as data obtained on any one date constrain the angular distance of HW1's pole direction from both the sky position and the antipodal position.

(Hudson and Ostro, 1999), hence the need to use this penalty function to explore our model's degree of flattening.

Finally, having established the pole direction and appropriate weights for the various penalty functions while assuming Lambert scattering in the microwave regime, we relaxed this assumption and estimated the exponent of the radar scattering law. We began with a grid search, trying several modeling runs – fitting first a three-ellipsoid model and then a vertex model – in which the exponent was held fixed at different values ranging from 1.0 (uniform brightness) to 8.0 (highly specular scattering). This grid search produced a broad χ^2 minimum centered at about 1.5 and ruled out values of 4 or greater. We then tried one more run in which we initialized the exponent at 1.0 but allowed SHAPE to fit its value rather than holding it constant. This run yielded a value of 1.4. Based on these results we estimate a scattering-law exponent of 1.5 ± 0.5.

4. Modeling results

4.1. Bifurcation

Our final model of HW1 is shown in Fig. 6 and its properties are listed in Table 3. We compare model predictions (synthetic data) to our actual delay-Doppler images, CW spectra, and lightcurves in Figs. 7–9, respectively. The fits to our images are quite good, and apart from a few stray points the lightcurve fits are good as well. The CW fits are somewhat less accurate but still do a good job of predicting the bandwidth, the overall shape, and (in most cases) the strength of our spectra. One problem is that in order to minimize rotational smearing each of our 16 modeled spectra is the incoherent sum of just 24 independent spectra ("looks"), so the noise is χ^2-distributed and somewhat "spikier" than would be
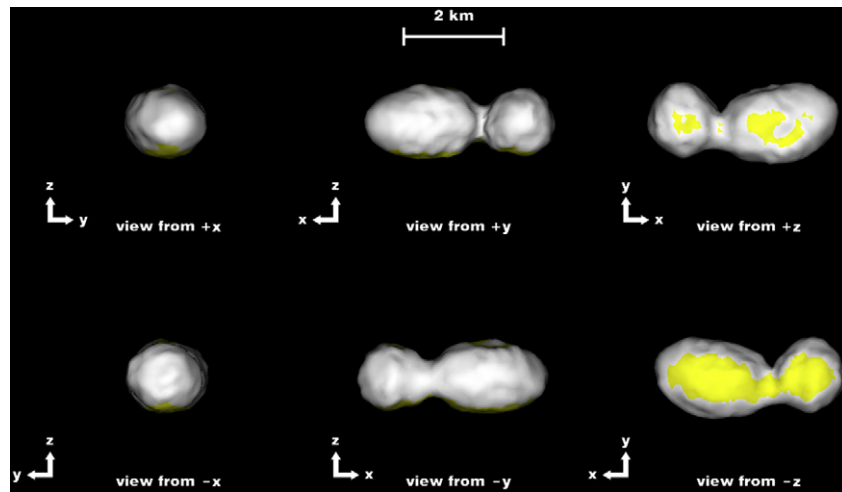
Fig. 6. Views of our best-fit HW1 model along its principal-axis directions. The rendering uses a Lambert backscattering law and has been effectively smoothed as described by Magri et al. (2007, Section 3.1.2); hence the triangular facets are not visible. Yellow-shaded regions are those that the *radar* never viewed or else viewed only at scattering angles greater than 60°, ensuring nonexistent or weak contributions to the radar images and spectra. (*Lightcurve* observers viewed the entire surface such that both the incidence angle and the scattering angle were less than 60°, except for one tiny region near the north pole.)

the case for a Gaussian distribution. (Alternatively, some of the spikes could be real features produced by topography smaller than the model's resolution.) Another problem is that our model predictions for the first two spectra on 15 September 2008 are weak but not as weak as the actual echoes. But we reiterate that in most respects the CW fits are reasonable.

The model is strongly bifurcated, with a pronounced "neck" separating two lobes. Thus HW1 is a contact binary, defined by Benner et al. (2006) as "an asteroid consisting of two lobes that are in contact, have a bimodal mass distribution, and that may once have been separate." The volume is 21% less than the volume of the model's convex hull; that is, our model has a "nonconvexity measure" of 0.21 in the terminology of Ďurech and Kaasalainen (2003). Those authors showed that lightcurves for such an object can be closely fit by a convex-definite model unless solar phase an-

gle exceeds 60°, well above the values for our HW1 lightcurves. We confirmed this with a modeling run that used only lightcurve data. Starting from a *single* ellipsoid we obtained a quasi-convex model that fit the lightcurves well, yet this alternative model yielded a terrible fit when we applied it to the radar images. (Fig. 10 illustrates this for the convex model from Section 3.1.) Thus we conclude that the presence of the neck in our best-fit model is required primarily by the radar images.

The near-equatorial radar view meant that echo power from high-latitude surface regions was weak (see Fig. 6), so these regions are less well constrained than the rest of the model. In principle one could therefore argue that instead of a continuous neck there might be two deep, narrow, parallel indentations running north–south on opposite sides of HW1 – that is, the asteroid is "pinched" in the direction perpendicular to its rotation axis but

Table 3
Properties of the model.[a]

Extents along principal axes (km)	x	3.78 ± 5%
	y	1.64 ± 10%
	z	1.49 ± 15%
Extent ratios	x/y	2.30 ± 10%
	y/z	1.10 ± 15%
Area (km²)		16.2 ± 15%
Volume (km³)		4.34 ± 25%
Volume of convex hull (km³)		5.47 ± 25%
Equivalent diameter of a sphere with the model's volume (km)		2.02 ± 8%
Ratios of the principal moments of inertia of a uniform-density asteroid with the model's shape	I_Z/I_X	5.01 ± 15%
	I_Z/I_Y	1.02 ± 5%
Dimensions of the dynamically equivalent equal-volume ellipsoid (DEEVE, the uniform-density ellipsoid having the same moment-of-inertia ratios and volume as the model) (km)	$2a$	4.20 ± 5%
	$2b$	1.48 ± 10%
	$2c$	1.33 ± 15%
Julian date when the positive side of the longest (x) principal axis is in the plane of the sky while approaching Earth		2454724.73693[b]
Angular radar scattering-law exponent n		1.5 ± 0.5
Equivalent spherical OC radar albedo		0.15 ± 0.04
Sidereal period (h)		8.76243 ± 0.00004
Pole ecliptic longitude (°)		281 ± 5
Pole ecliptic latitude (°)		−31 ± 5

[a] Listed uncertainties on tabulated quantities are conservatively assigned standard errors: the modeling process inevitably involves many subjective judgment calls – see Section 3.4 of Magri et al. (2007) and Section 4 of Ostro et al. (2010) – so we try to err on the side of larger error estimates. For example, the first step in estimating uncertainties on the model's physical dimensions was to consider the models produced during our pole-direction grid searches (see Section 3.2.2): we computed the spread (standard deviation) in parameter values for the subset of models that yielded reasonable fits to the data. Then, because "reasonable fit" is a subjective criterion that relies as much on visual inspection as on reduced χ^2 values, we substantially increased these error estimates, resulting in the values tabulated above. We carried out a multirun grid search using different values of angular radar scattering-law exponent n in order to estimate this parameter and its standard error. The standard error on the equivalent spherical OC radar albedo is dominated by the 25% systematic calibration uncertainty on measured OC cross sections.
[b] This epoch corresponds to 05:41:10 UT on 15 September 2008. The light from this event reached Earth at JD 2454724.73771 (05:42:18 UT on 15 September 2008).

not in the direction parallel to the rotation axis. However, this scenario strikes us as implausible, whereas a continuous neck could easily result from two initially separate bodies coming into contact with each other.

While our model clearly fits the data well, one may question whether it is unique: is bifurcation truly *required* by the data? As was mentioned in Section 3.2.3, for some modeling runs we used the "concavity" penalty function to see if we could remove the neck between the lobes, finding that we could not. In order to address the existence of a neck more directly we then carried out new runs using the "bifurcation" penalty function. This function divides the model into ten equal-width zones along its long axis and computes S, the mean squared distance from this axis,

for the vertices in each zone. It then identifies the model's deepest neck by looking for three zones z_1, z_2, and z_3 (where z_2 lies somewhere between z_1 and z_3) for which the ratio $r = 2S_2/(S_1 + S_3)$ is minimized. The penalty function is then set equal to $(1/r - 1)^2$, so that the value is large for highly bifurcated models; for a nonbifurcated model with $r > 1$ the penalty is instead set to zero. Again we found that SHAPE refused to remove the model's neck – particularly the deep indentation on the upper side of the "view from +z" in Fig. 6 – even when the bifurcation penalty came close to doubling the objective function that SHAPE tries to minimize. Yet another method of addressing this issue is described in the Supplementary material. We conclude that our data do indeed require a bifurcated model.
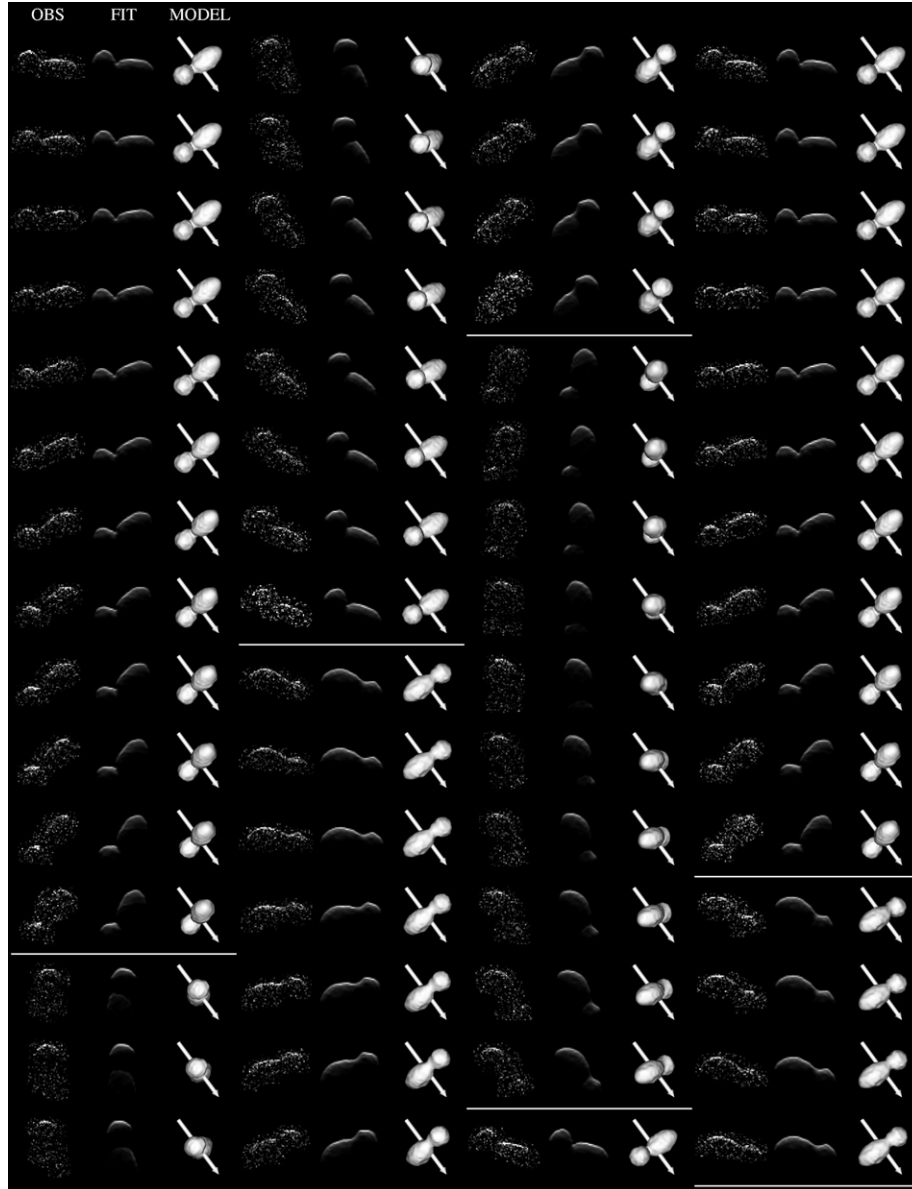

Fig. 7. HW1 delay-Doppler images and model. Every second OC image is displayed, with the corresponding synthetic image from the model fit shown to its right, and the corresponding plane-of-sky (POS) rendering of the shape model shown to the right of the synthetic image. The actual and synthetic delay-Doppler images have the same orientation, pixel dimensions, and overall dimensions as do the images displayed in Fig. 1. Here, however, many noise pixels in the actual images have been masked out (see Section 3.2.1) and appear black, causing the image outlines to appear irregular. The grayscales for the actual and synthetic images have the same maxima, with radar cross section values of 0.009 km² per pixel or more mapping to bright white. To enhance visual clarity the grayscale for the actual images has been set to deemphasize low-level noise; this has not been done for the synthetic images in order to display the weak features that could be observed in the limit of noise-free data. In the POS frames, north is up and east is to the left. Each POS frame is 5.0 km on a side, and each pixel is 0.025 km on a side. The sidereal spin vector is denoted by an arrow. POS renderings use Lambert scattering, producing somewhat stronger limb-darkening than would the best-fit radar scattering law (see Table 3). In each panel time increases from top to bottom and then from left to right; the end of each of the six observing dates (see Table 1) is marked by a horizontal white line. The final images obtained on 15 and 19 September have been omitted from the figure.
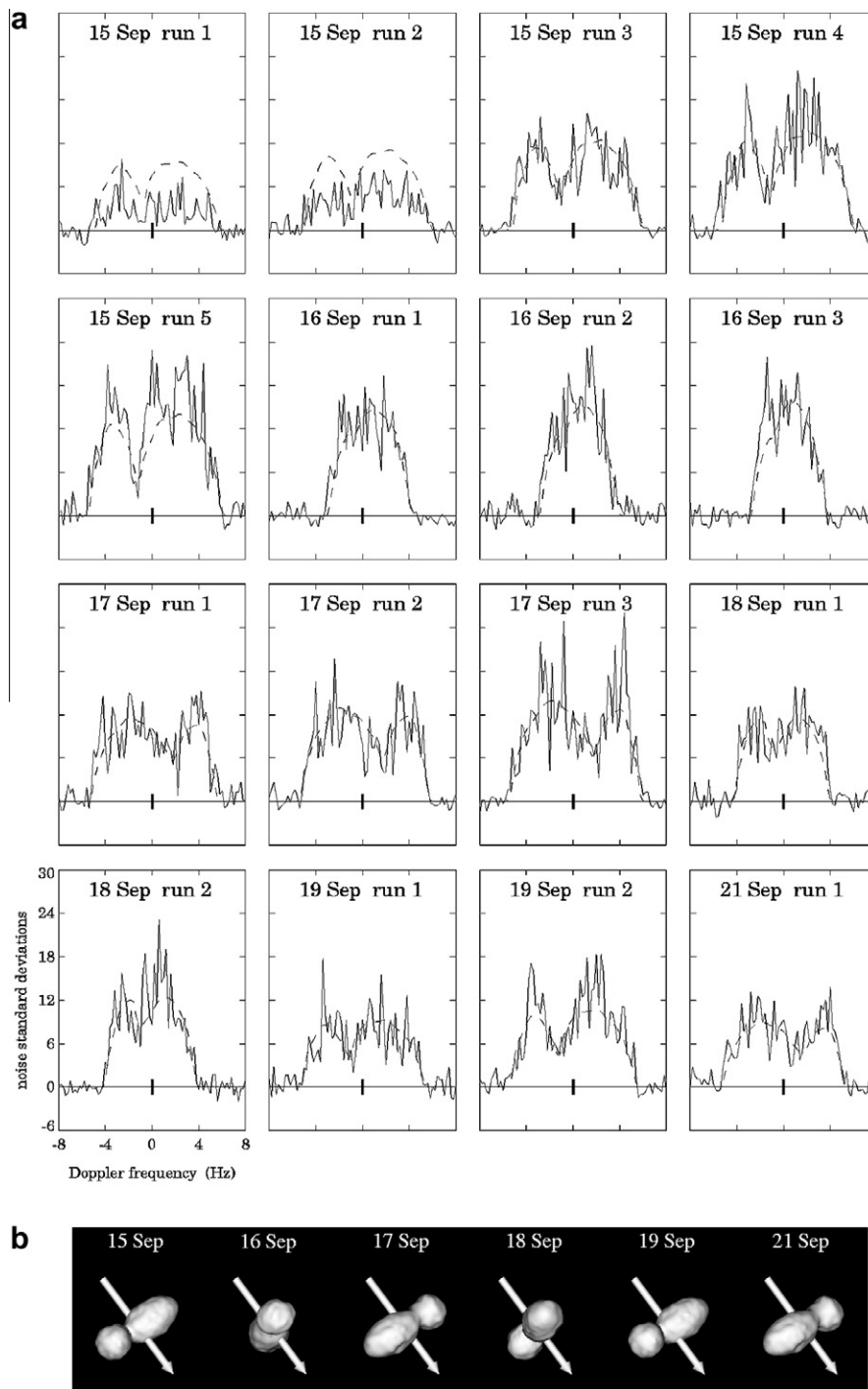
Fig. 8. HW1 CW spectra and model. (a) Echo power, in units of standard deviations of the noise, is plotted vs. Doppler frequency (Hz) relative to that of hypothetical echoes from the target's center of mass. Each of the sixteen OC spectra is displayed as a solid line, with the corresponding synthetic spectrum from the model fit superimposed as a dashed line. All plots have identical axis scales, shown on the plot at lower left. The vertical bar at the origin indicates ±1 standard deviation of the noise. Each label gives the 2008 observing date and the CW run number on that date. All spectra are displayed at the raw frequency resolution of 0.20 Hz. (b) Plane-of-sky (POS) renderings of the shape model at or near the midpoint of the CW observations for each of the six observing dates. Each rendering's size, orientation, and adopted scattering law is the same as for the POS views in Fig. 7.

4.2. Other results

Another salient feature of our HW1 model is its high degree of elongation. With the ratio of its maximum equatorial dimensions ~2.3, HW1 is the fourth most elongated radar-observed NEA, after (1620) Geographos, (11066) Sigurd, and (4179) Toutatis. (The mean elongation and r.m.s. dispersion for 37 radar-observed NEAs is 1.49 ± 0.46; see http://echo.jpl.nasa.gov/~lance/nea_elonga-tions.html for a listing.) The model's flattening is less well constrained than its elongation, given that the radar had a near-equatorial view and that all lightcurve views were within 35° of the equator. By using penalty functions to investigate the
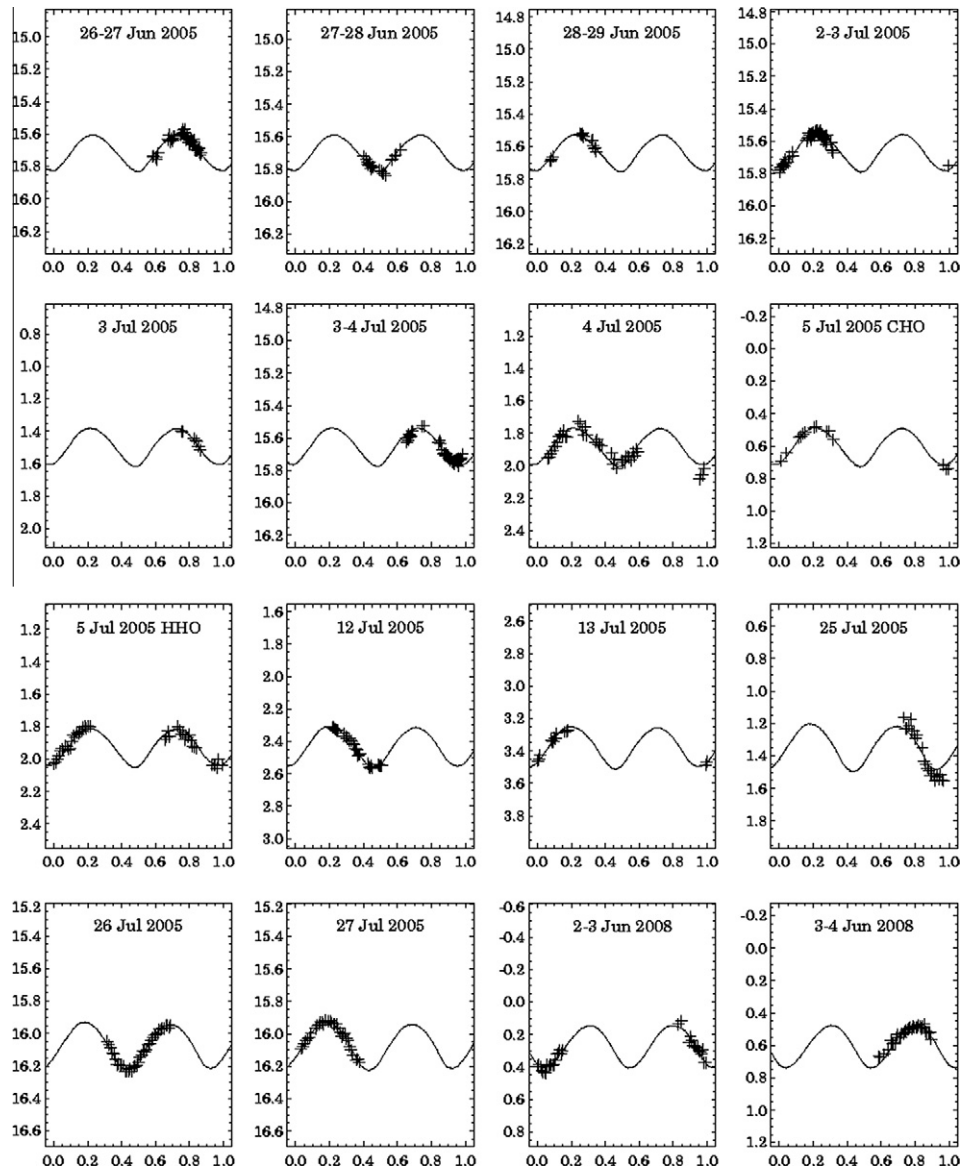
Fig. 9. HW1 lightcurves and model. The x-axis represents rotation phase, with plane-of-sky motion taken into account and the zero-phase epoch as given in the notes to Table 1. Units on the y-axis are magnitudes, although our modeling software minimized χ^2 in intensity space rather than magnitude space. Each plot spans 1.50 mag. Data points for each lightcurve are displayed as crosses and the corresponding synthetic lightcurve is displayed as a solid curve. No correction for solar phase angle has been applied to the data. Each lightcurve is labeled by the observing date and, in cases of multiple lightcurves on the same date, by the photometric filter (for absolute photometry), the observatory (CHO = Carbuncle Hill, HHO = Hunters Hill), or a sequence number (for lightcurves obtained at the same observatory).

flattening (see Section 3.2.3), we have determined that the ratio of the intermediate to short (polar) dimensions is 1.10 ± 0.15; thus HW1 is unlikely to be more than moderately flattened.

Most of the model's surface has a low gravitational slope, defined as the angle that a plumb line would make with the local surface normal. Because we used penalty functions to suppress facet-scale topography, these shallow slopes may be a modeling artifact rather than a sign that the surface is truly relaxed. Some parts of the surface near the model's neck and on the smaller component have gravitational slopes between 35° and 67°, above the typical angle of repose for loose material; steep slopes are unlikely to be an artifact, so these regions may represent exposed regolith-free rock.

As discussed in Section 3.1, a spin vector and a convex-definite shape model have been determined via lightcurve inversion using data obtained at Table Mountain. The model presented in Section 3.2 is based on both these and additional lightcurves and, of course, on radar data; yet the convex model's pole position at (282°, −39°) is within 10° of our best-fit value at (281°, −31°),

and its shape is a reasonable approximation to the 3D convex hull of the radar-and-lightcurve-based model (not shown). Thus, in this instance at least, we confirm that lightcurve-based inversions are able to produce a robust spin vector estimate even when the actual shape is not at all convex-definite. Lightcurve observations typically cover a larger range of viewing geometry than do radar observations and thus better constrain the pole direction and axis ratios. However, if we use the convex model to generate radar predictions (Fig. 10) we see that the radar data provide evidence for topographical features, such as the neck, that are not detectable from the lightcurve data alone. Hence we also confirm that radar observations are valuable for determining an asteroid's actual shape. The combination of radar and lightcurve data provides a better model than does either kind of data alone.

Given our model and an assumed bulk density we can investigate the orbits of hypothetical bodies near the asteroid. HW1 exhibits the general pattern described by Scheeres et al. (1996) in that it has four synchronous orbits in its vicinity – that is, four
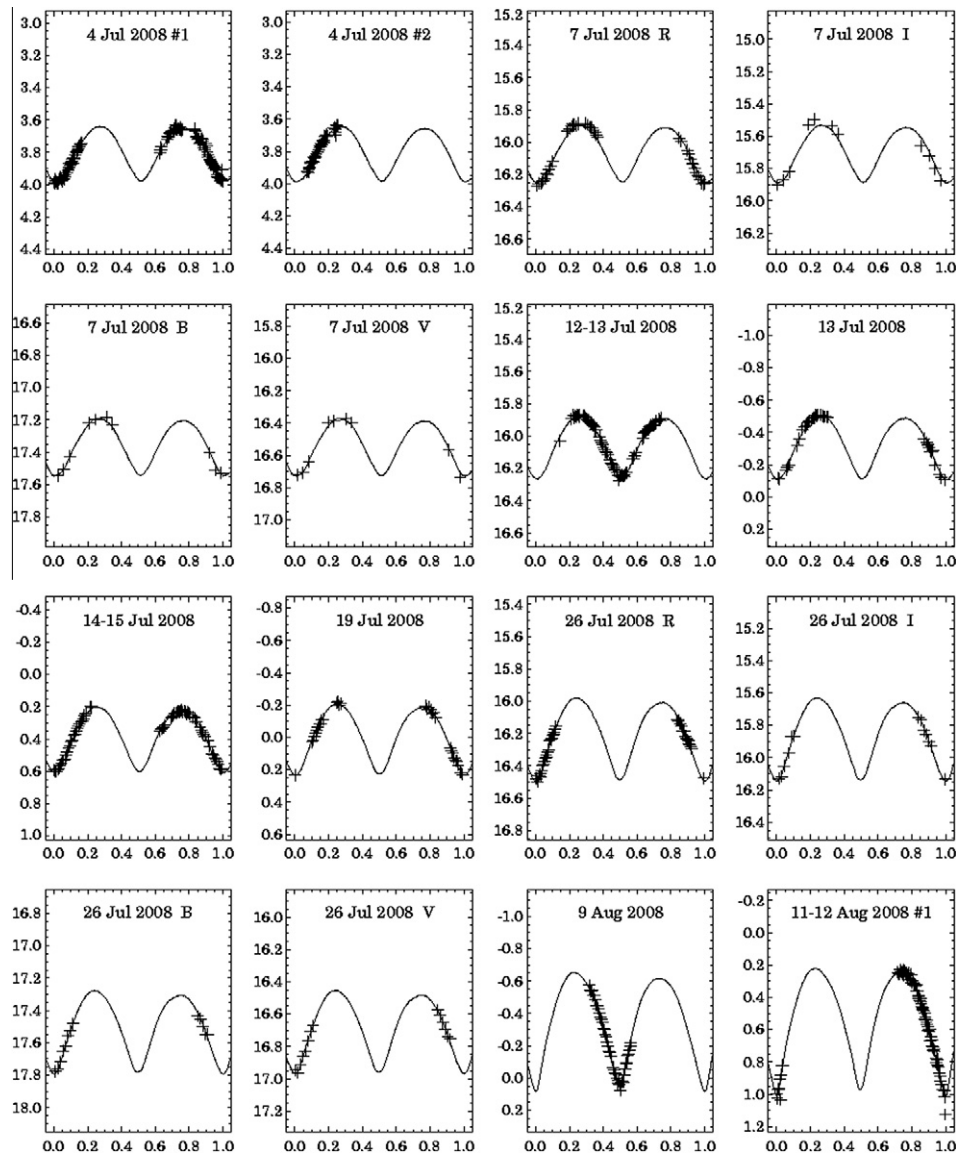
Fig. 9 (*continued*)

circular orbits, lying in HW1's equatorial plane, for which the orbital motion is synchronous with HW1's rotation rate. For our nominal bulk density we choose 2.0 g cm^{-3}, the mean of the four estimates listed by Consolmagno et al. (2008) for individual S-class NEAs. (This value corresponds to a macroporosity of 40%, assuming L-chondritic composition and using the mean bulk density of 3.37 g cm^{-3} quoted by Consolmagno et al. for L-chondrite meteorite falls.) We find that all four synchronous orbits are unstable for our nominal bulk density. HW1 has a relatively strong elongation, indicative of highly unstable orbital dynamics within a few mean radii. Fig. 11 shows the placement of orbital equilibria about the body, overlain with lines of constant geopotential (Scheeres et al., 1996). Increasing the bulk density by a few tens of percent would move the four equilibrium points slightly outward but would not stabilize them, while decreasing the bulk density moves the equilibrium points inward and makes them even more strongly unstable.

By combining the OC and SC cross sections from our disk-integrated CW data (Fig. 12) with model-based projected areas, we obtain an OC radar albedo of 0.16 ± 0.04 and a circular polarization ratio of 0.29 ± 0.03 (Table 4). There is no evidence for significant rotational variation in either quantity. These two values are quite similar to those obtained for (25143) Itokawa, 0.16 ± 0.05 and 0.26 ± 0.04 (Ostro et al., 2004), and in fact they are typical for S-class NEAs. (See http://echo.jpl.nasa.gov/~lance/asteroid_radar_properties/nea.radaralbedo.html for a compilation of OC albedos and Benner et al. (2008) for polarization ratios.) HW1's OC albedo is characteristic of a rocky object with lunar-like porosity (Shepard et al., 2010). Its polarization ratio implies a moderate degree of decimeter-scale structure within a meter or so of the surface, but we must be cautious in our interpretation: (433) Eros has a polarization ratio of 0.28 ± 0.06, similar to that of Itokawa (and HW1), yet spacecraft images show that Eros's surface is very different from Itokawa's at decimeter scales.

Because the shape modeling process includes fitting corrections to the *a priori* delay-Doppler ephemeris predictions, we were able to use these corrections to update HW1's heliocentric orbit. The revised orbit solution is presented in Table 5. Orbital element uncertainties were reduced by about 27% by the inclusion of our twelve radar astrometry points (one delay measurement and one Doppler measurement per observing date). Given that the *a priori* solution relied on a half-century of optical data, including precovery images
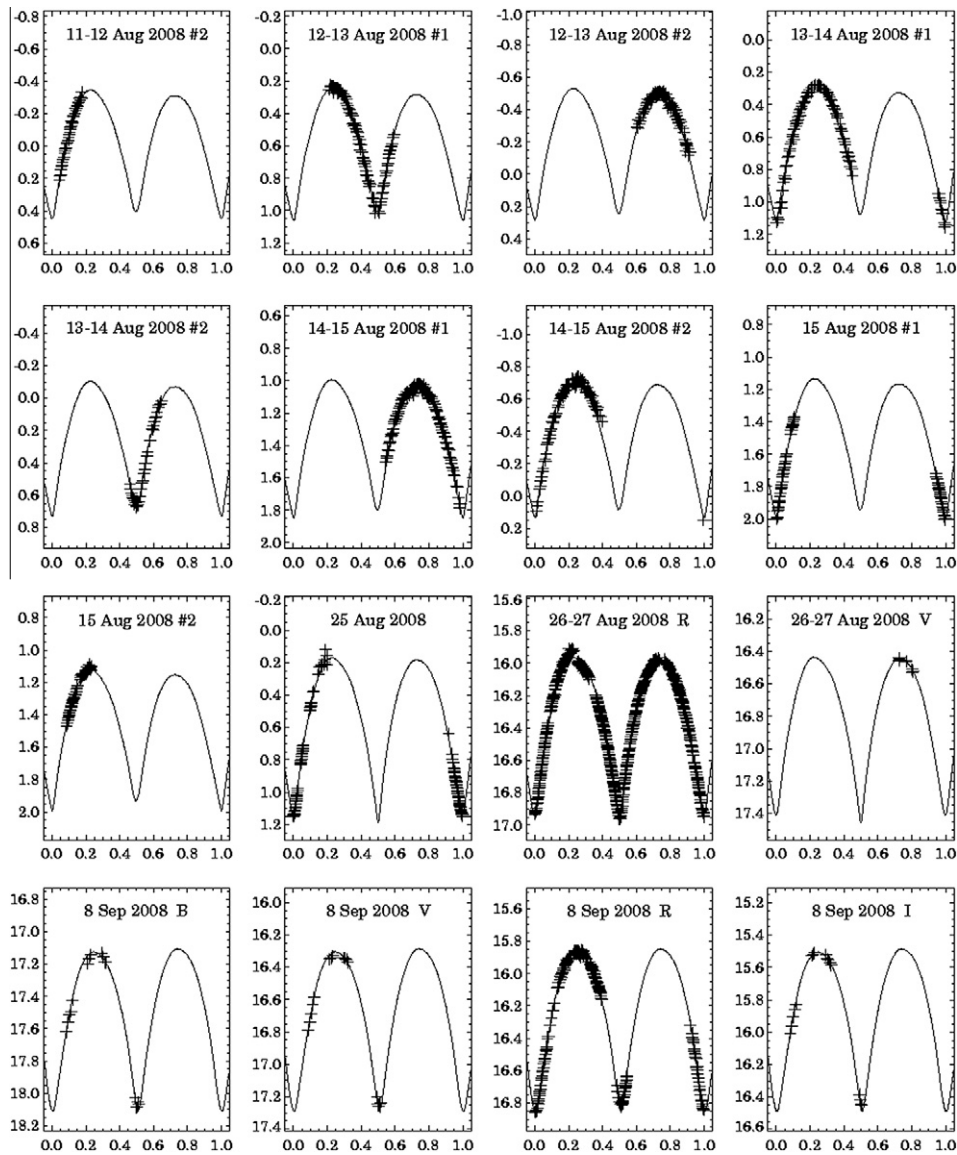
Fig. 9 (*continued*)

dating as far back as 1955 (the Palomar Sky Survey), this is a significant improvement. The revised solution implies that between A.D. 200 and A.D. 3000 the asteroid has no encounters with planets, (1) Ceres, or (2) Pallas closer than 0.1 AU and no encounters with (4) Vesta closer than 0.05 AU.

5. Discussion

5.1. Current geophysical state and possible past evolution

The clear contact-binary features of HW1 can be analyzed using a simple model that assumes an ellipsoid for the body and a sphere for the head (Scheeres, 2007b). For the current rotation period of 8.76243 h and an assumed bulk density of 2.0 g cm^{-3} (see Section 4.2) the system is not in a minimum energy state, implying that there must be internal strength between the apparent head and body to sustain the current geometry: the asteroid's neck is under compression and supports a transverse shear force. Using this simple model with the assumed bulk density indicates that a rotation period of approximately 7.4 h would make the current configuration a minimum energy configuration. A rotation period

of approximately 5.7 h would place the two components in orbit about each other. The significant rotation periods listed here scale inversely with the square root of bulk density (Scheeres, 2007b); thus a bulk density of 1.43 g cm^{-3} makes the current configuration a minimum energy configuration and a bulk density of 0.85 g cm^{-3} places the current system at its fission rotation rate.

None of the four bulk density estimates quoted for S-class NEAs by Consolmagno et al. (2008) is as low as the 1.43 g cm^{-3} required to put HW1 into a minimum energy configuration given our current model. Given the compositional assumptions made in Section 4.2, this bulk density corresponds to a macroporosity of 58%, at the upper limit of the range depicted for NEAs in Fig. 7 of Consolmagno et al. Although such a high macroporosity is not out of the question – for example, the range of plausible porosities (including microporosity) for the primary "alpha" component of S-class NEA (66391) 1999 KW4 is between 40% and 66% (Ostro et al., 2006) depending on that object's composition – it is much more likely that HW1 is denser than this and hence that it is not in a minimum energy state.

HW1's spin rate is likely to be evolving owing to the YORP effect, a torque caused by asymmetric thermal re-radiation of ab-
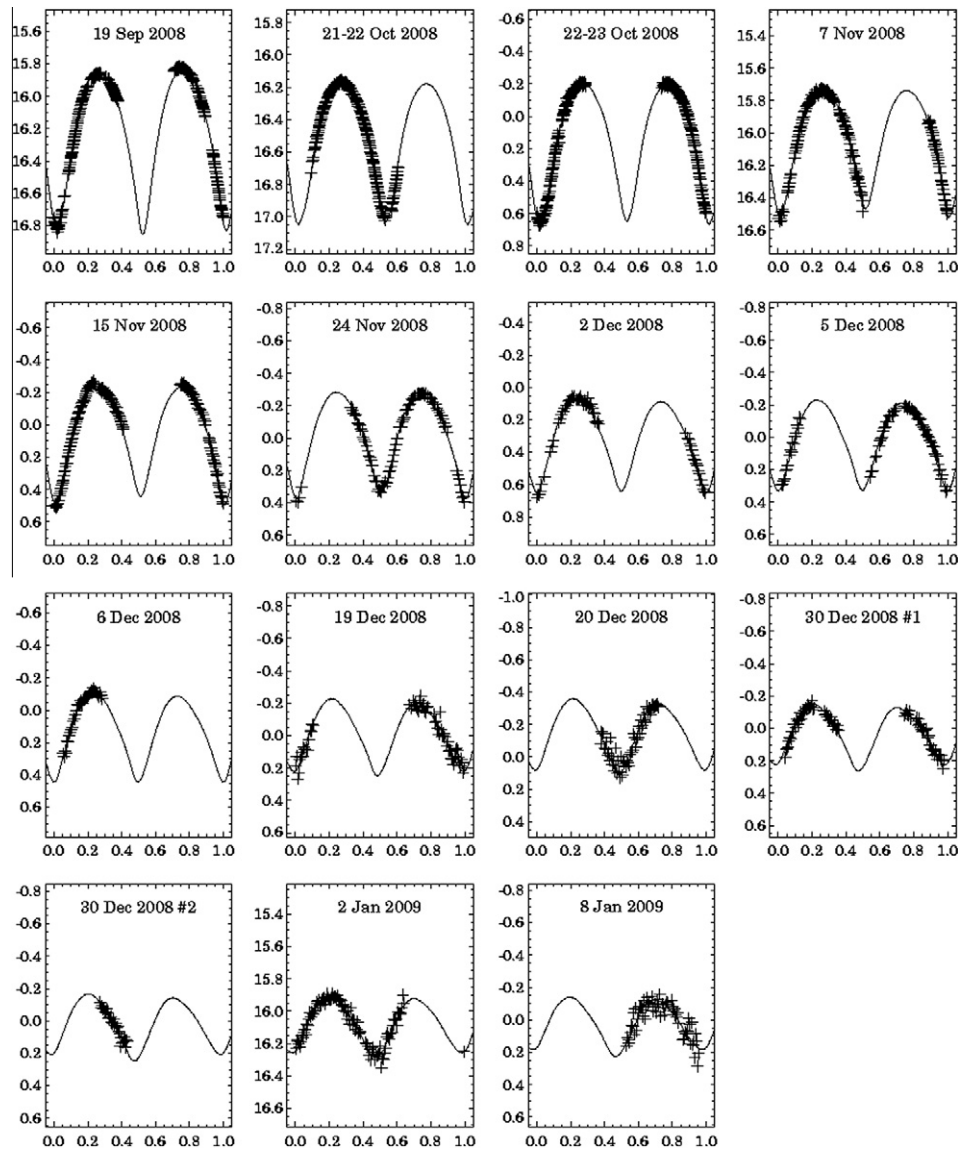
Fig. 9 (*continued*)

sorbed sunlight from an irregularly shaped body (Rubincam, 2000). Direct use of the current shape model, following the approach described by Scheeres (2007a), indicates that the body is currently slowing in its rotation rate. The value of this YORP deceleration cannot be precisely computed because of hectometer-scale surface inaccuracies in our model – in particular, unknown north–south asymmetries. We suppressed small-scale topography in our model (see Section 3.2.3), and YORP is extremely sensitive to such surface detail (Scheeres et al., 2007; Statler, 2009). Hence there is considerable uncertainty in the rate at which this asteroid's spin rate is decreasing.

Assuming that HW1 was spinning more rapidly in the past, potentially at its spin fission limit, raises the possibility that the components of the asteroid have been in orbit about each other at some point in time. It is important to note that, should the given shape undergo a spin fission and enter a mutual orbit, the mass fraction of the secondary to the total system mass (assuming constant density) is 0.33, implying that the resultant binary system would have a negative free energy (Scheeres, 2009) and the components would be unable to escape from each other. Thus, this is

consistent with the current body being captured into a contact binary state. Such a system could have existed as a stable binary asteroid for some period of time, however, raising interesting questions about the pathway for forming a contact binary.

Taylor (2009a,b) modeled the interplay between the YORP effect and the tidal evolution of a binary system. If YORP happens to be slowing down the primary component's rotation, it drains angular momentum from the system, altering the orbital separations of the fully synchronous tidal end states. Eventually the system is left in a configuration where a stable, fully synchronous tidal end state is unattainable via tidal evolution, which forces an eventual merger of the components. The timescale for this orbital evolution depends strongly on the relative masses of the two components: equal-mass systems can merge within tens of thousands of years, whereas those with two very different masses can take two or more orders of magnitude longer. Our HW1 model suggests that the two original components, now joined at the narrow neck, were in a roughly 1:2 secondary-to-primary mass ratio, not equal but not strongly different. Hence it is plausible that such a system could decay and merge within 1 Myr, well within the typical 10-Myr NEA lifetime.
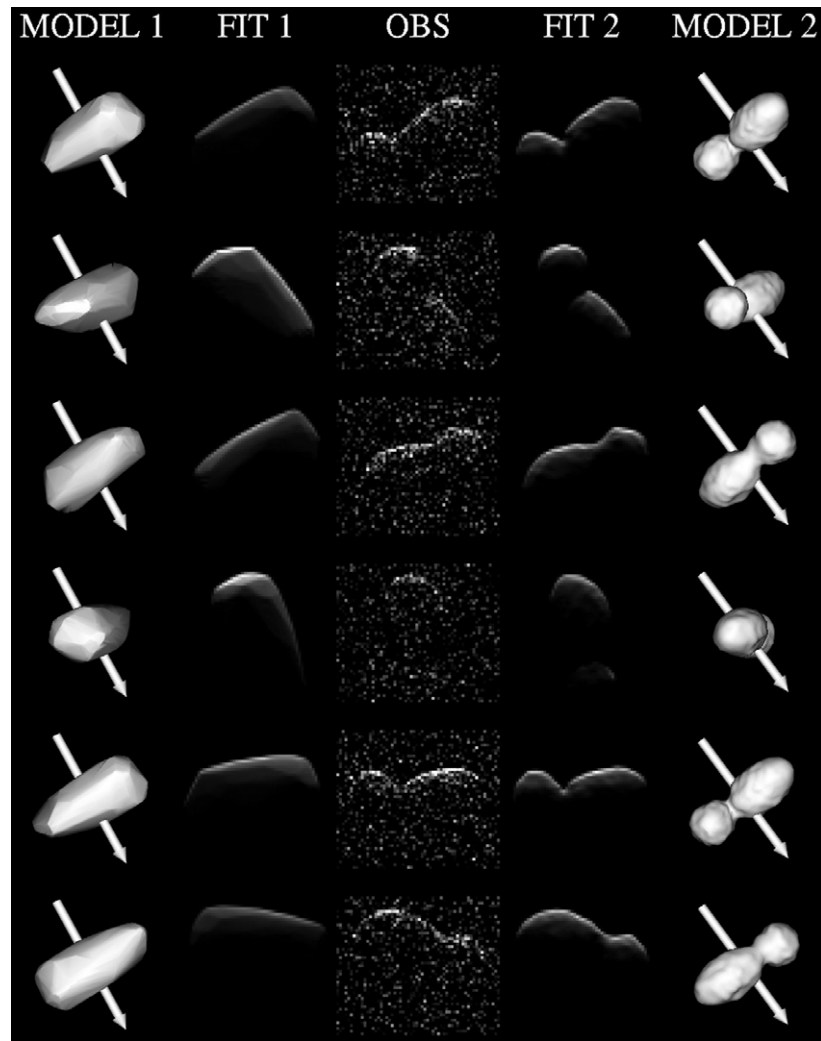
Fig. 10. HW1 delay-Doppler images as fit by two different models. The center column displays six OC images, each one selected from near the middle of one of the six observing dates; time increases from top to bottom. The leftmost two columns show the corresponding plane-of-sky renderings of the lightcurve-based convex-definite shape model from Section 3.1 and the synthetic images derived from that model, while the rightmost two columns show the same information for the radar-and-lightcurve-based model from Section 3.2. Because the convex model has no intrinsic linear scale we have scaled it so that the two models have the same maximum diameter. The size and orientation of each image is the same as for the images displayed in Fig. 7. Grayscales are also the same except that the convex model's synthetic images have been scaled in brightness by an arbitrary factor, as radar reflectivity was not estimated for that model. The sidereal spin vector is denoted by an arrow. The convex model cannot adequately represent prominent features in delay-Doppler space (the center column) that result from our viewing concavities in HW1 (as seen in the rightmost column).

The hypothesized Binary YORP (BYORP) effect could also have influenced the evolution of this system. In this effect solar radiation pressure and re-emission acting on a synchronously rotating secondary can cause the orbit to expand or to shrink over time-scales of 100,000 years (Ćuk and Burns, 2005; Ćuk, 2007). Whether the orbit expands or shrinks is controlled by the orientation of the secondary to the primary, with growth leading to a circularization of the orbit and contraction leading to an increase in eccentricity (McMahon and Scheeres, 2010). Ćuk and Nesvorný (2010) hypothesize that expansion is likely to end in a bout of chaotic rotation followed by inward evolution rather than in dissociation of the system, but the detailed mechanisms of the long-term evolution of these systems have not yet been fully solved. It is clear, however, that the BYORP effect could have caused the system to form into a contact binary after a period of existence as a stable binary asteroid.

5.2. Future observations

In principle we could improve upon the current HW1 model and reduce the uncertainty on our YORP estimate by obtaining new radar images. Unfortunately, all radar opportunities for the remainder of this century will be weak, suitable for obtaining CW spectra but not delay-Doppler images. Spectra are much less useful for modeling than images and thus will provide few new constraints on our model. Not until 22 September 2242 will HW1 again come as close as it did in 2008, approaching to within 0.123 AU of Earth. In the meantime we will have to rely on additional lightcurve measurements, especially at high subobserver latitudes, to refine the model presented here. Such opportunities will occur, for example, in late 2011 (with subobserver latitude roughly +40°, apparent visual magnitude ~16.3, and solar elongation ~130°) and in September–October 2046 (roughly −50°, 13.9 mag, and 120°).

5.3. Comparison with similar asteroids

In order to place HW1 in context we use Table 6 to compare it to six other asteroids – a main-belt object and five NEAs – whose published shape models display a significant degree of bifurcation. The table lists two relevant quantities for each model of each asteroid. One, the nonconvexity measure (see Section 4.1), is an indirect
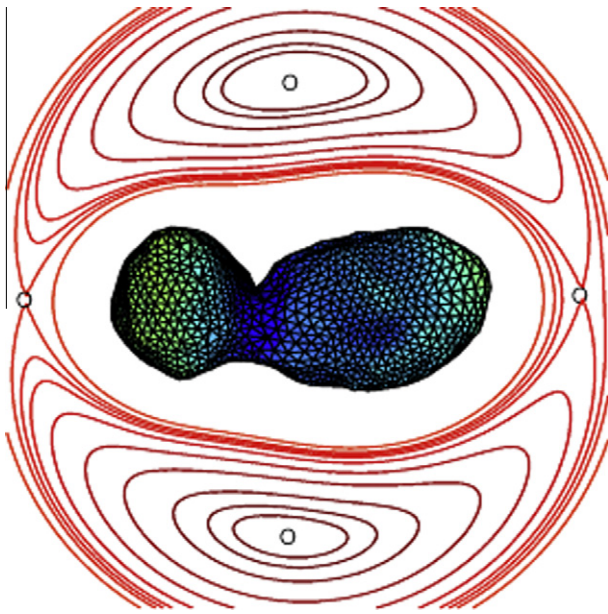
Fig. 11. Pole-on view of HW1 showing the locations of the four synchronous orbital equilibria in the equatorial plane, overlain on a contour plot showing values of the geopotential above and on the surface of HW1. A hypothetical particle placed at any of these equilibrium points with zero speed in the co-rotating HW1 frame will experience a net zero acceleration in the co-rotating frame and, in an inertial frame, would describe a circular orbit exactly synchronous with HW1's rotation rate. For HW1 all four of these circular orbits are unstable, meaning that any particle placed in such an orbit would not remain in that orbit indefinitely. The geopotential for HW1 is the sum of the gravitational potential plus the rotational potential. The lowest point of the geopotential on the model's surface (depicted in blue) is located in the area between the components, while the highest points on the geopotential (depicted in green) occur at the ends of the asteroid.

Fig. 12. Weighted sum of all OC (solid line) and SC (dashed line) CW echo spectra obtained for HW1. Echo power, in units of standard deviations of the noise, is plotted vs. Doppler frequency (Hz) relative to that of hypothetical echoes from the target's center of mass. The vertical bar at the origin indicates ±1 standard deviation of the OC noise. Both spectra have been smoothed from the raw frequency resolution of 0.20 Hz to an effective resolution of 0.50 Hz. Rotation phase coverage is depicted in the upper right portion of the plot. Each radial line segment denotes the phase (defined as in Table 1) of a single run; the length of the segment is proportional to the noise standard deviation of the corresponding OC spectrum. Phase increases counterclockwise, with zero phase marked by the arrow at the three o'clock position.

indicator: a bifurcated body necessarily has large concavities but the converse need not be true. For reference, the nonconvexity measure of a convex-definite object is zero, that of a pair of barely touching identical spheres is 0.20 (roughly the same value obtained for HW1), and that of a pair of identical, coaligned right circular cones touching at their tips is 2/3. We see that HW1 is significantly more nonconvex than (2063) Bacchus, (4179) Toutatis, (4769) Castalia and (25143) Itokawa and is similar to (4486) Mithra. Only the "dog bone" model of (216) Kleopatra (Ostro et al., 2000), whose volume is 36% less than the volume of the model's convex hull, exhibits much larger concavities than does HW1.

As a more direct measure of bifurcation we employ the value of the "bifurcation" penalty function defined in Section 4.1. By this criterion HW1 is much more strongly bifurcated than the five comparison NEAs, even the 2-lobe model of Bacchus (Benner et al., 1999) with its central neck. (It should be noted that the Bacchus
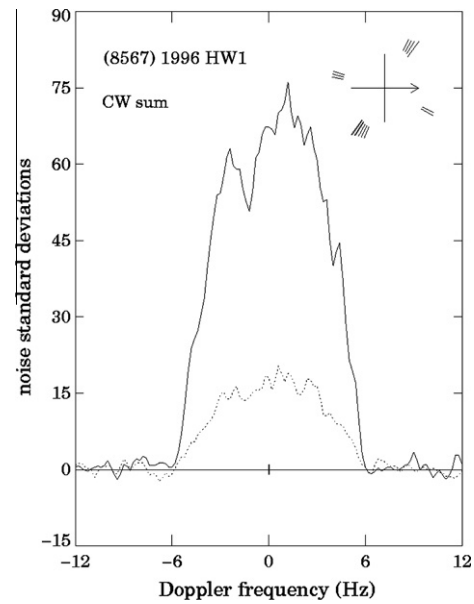
data were somewhat weak and hence the models, particularly the 2-lobe model, have significant uncertainties.) The low bifurcation penalty obtained for Itokawa highlights the fact that this NEA's "neck" is defined more by bending than by narrowing. Only Kleopatra approaches HW1's degree of bifurcation as judged by this criterion. Of course the formation mechanisms for Kleopatra, a 111-km metallic main-belt asteroid, and HW1, a 2-km NEA, may be quite different. Restricting our attention to small NEAs, we conclude that although Castalia has often been thought of as a prototypical contact binary, HW1 is in fact more bifurcated than any other NEA whose shape has been modeled.

Currently there exist more radar datasets than radar-based models, and there are strong indications that HW1 is not alone. For example, 2005 CR37 (Benner et al., 2006) was not observed extensively enough to support a shape model, but the radar images imply an elongated object with a deep, wide concavity on one of its

Table 4
Disk-integrated radar properties.

Observing date (UT)	CW runs	Subradar lat., long. (°)	OC SNR	σ_{OC} (km^2)	Proj. area (km^2)	$\hat{\sigma}_{OC}$	μ_C
15 September 2008	5	+9, 119	140	0.590	4.06	0.145	0.29
16 September 2008	3	+9, 195	122	0.416	2.63	0.159	0.32
17 September 2008	3	+9, 299	125	0.655	4.06	0.161	0.29
18 September 2008	2	+9, 28	88	0.471	3.05	0.154	0.31
19 September 2008	2	+9, 124	84	0.654	3.95	0.166	0.32
21 September 2008	1	+9, 306	53	0.661	3.93	0.168	0.23
Adopted values and standard errors						0.16 ± 0.04	0.29 ± 0.03

Notes: For each radar observing date we list the date; the number of CW runs on that date; the mean subradar latitude and longitude during those runs; the signal-to-noise ratio of the weighted sum of OC spectra; the OC cross section σ_{OC}; the mean projected area according to our model; the OC albedo $\hat{\sigma}_{OC}$; and the circular polarization ratio $\mu_C \equiv SC/OC$. Subradar longitude is east longitude measured from the body-fixed +x-axis (which is very close to the +x principal axis of inertia, see Fig. 6) and is equal to 360° minus the rotation phase listed in Table 1. Adopted values of $\hat{\sigma}_{OC}$ and μ_C are unweighted means of single-date values. The standard error on our adopted circular polarization ratio reflects date-to-date variations; the standard error on our adopted OC albedo also reflects 25% calibration uncertainty.

Table 5
(8567) 1996 HW1 orbital solution (#233).

J2000 heliocentric ecliptic coordinates Epoch 2455594.50000 = 2.0 February 2011		
Osculating element	Value	Formal 1-sigma error
Eccentricity	0.4490584916 ± 0.0000000069	
Perihelion distance	1.127125303 ± 0.000000012 AU	
Time of perihelion	2455792.459203 JD ± 0.000010 d (18.95920 August 2011)	
Longitude of ascending node	177.1816703 ± 0.0000093°	
Argument of perihelion	177.095705 ± 0.000014°	
Inclination	8.4393049 ± 0.0000035°	
Semi-major axis	2.045816636 ± 0.000000014 AU	
Orbit period	1068.805021 ± 0.000011 d (2.9261773960 year)	
Mean anomaly	293.32243784 ± 0.00000062°	

Notes: The optical data consisted of 2474 usable measurements (1955–2010), with post-fit residual mean and r.m.s. of (0.147, 0.602) arcsec. The optical normalized r.m.s., obtained by first dividing each optical measurement by its assigned uncertainty, is 0.445. We incorporated into the orbital solution six radar delay measurements and six radar Doppler measurements, one of each per observing date; these measurements are tabulated at http://ssd.jpl.nasa.gov/?radar along with other asteroid radar astrometry. The post-fit residual mean and r.m.s. for our radar measurements are $(-0.065, 0.541)$ µs and $(-0.062, 0.069)$ Hz, and the delay and Doppler normalized r.m.s. values are 0.488 and 0.184, respectively. The combined optical-plus-radar normalized r.m.s. is 0.444.

Table 6
Comparison to other bifurcated asteroid models.

Name	Model	Equiv. diam. (km)	Volume (km³)	Nonconvexity measure	Bifurcation penalty	References
(216) Kleopatra		111	710,000	0.36	3.51	Ostro et al. (2000)
(2063) Bacchus	(1-lobe model)	0.64	0.14	0.09	0.03	Benner et al. (1999)
	(2-lobe model)	0.71	0.18	0.12	1.21	
(4179) Toutatis		2.45	7.68	0.11	0.00	Hudson et al. (2003)
(4486) Mithra	(Prograde model)	1.69	2.53	0.23	0.99	Brozović et al. (2010)
	(Retrograde model)	1.75	2.79	0.23	0.94	
(4769) Castalia		1.08	0.67	0.08	0.11	Hudson and Ostro (1994) and Hudson et al. (1997)
(8567) 1996 HW1		2.02	4.34	0.21	4.53	This paper
(25143) Itokawa		0.32	0.018	0.14	0.19	Gaskell et al. (2006)

Notes: The properties of our HW1 model as compared to those of eight other shape models of six other bifurcated asteroids. Listed quantities are the asteroid name; the particular model for targets with two different published models; the equivalent diameter of a sphere with the model's volume; the volume; the nonconvexity measure, defined by Ďurech and Kaasalainen (2003) as 1 − volume/(convex hull volume); the value of the "bifurcation" penalty function defined in Section 4.1; and the references.

broad sides (the only one observed). These images are remarkably similar to those shown for HW1 in Fig. 1, suggesting a similarly bifurcated object. Fifteen additional examples, radar targets such as (11066) Sigurd (Benner et al., 2004) and (141593) 2002 HK12 (Scoles et al., 2005), are listed in Table 9 of Brozović et al. (2010). In fact Benner et al. (2006) estimate that 10% of all NEAs larger than 200 m in diameter are candidate contact binaries. As our radar systems, computing hardware, and modeling software continue to improve, and as supporting lightcurve campaigns involving professional and skilled amateur observers become more common, we can expect to model a growing number of such asteroids in the years ahead.

Appendix A. Supplementary material

Supplementary data associated with this article can be found, in the online version, at doi:10.1016/j.icarus.2011.02.019.

References

Benishek, V., Protitch-Benishek, V., 2009. CCD photometry of asteroids at the Belgrade Astronomical Observatory: 2008 January–September. Minor Planet. Bull. 36, 35–37.
Benner, L.A.M. et al., 1999. Radar observations of Asteroid 2063 Bacchus. Icarus 139, 309–327.
Benner, L.A.M. et al., 2004. Radar imaging of near-Earth Asteroid 11066 Sigurd. Bull. Am. Astron. Soc. 36, 1143.
Benner, L.A.M. et al., 2006. Near-earth Asteroid 2005 CR37: Radar images and photometry of a candidate contact binary. Icarus 182, 474–481.
Benner, L.A.M. et al., 2008. Near-Earth asteroid surface roughness depends on compositional class. Icarus 198, 294–304.
Birlan, M. et al., 2009. Physical characterization of asteroids candidates of Marco Polo mission. Bull. Am. Astron. Soc. 41, 1061–1062.
Brozović, M. et al., 2010. Radar observations and a physical model of contact binary Asteroid 4486 Mithra. Icarus 208, 207–220.
Bus, S.J., Binzel, R.P., 2002. Phase II of the small main-belt asteroid spectroscopic survey: A feature-based taxonomy. Icarus 158, 146–177.
Consolmagno, G.J., Britt, D.T., Macke, R.J., 2008. The significance of meteorite density and porosity. Chem. Erde 68, 1–29.
Ćuk, M., 2007. Formation and destruction of small binary asteroids. Astrophys. J. 659, L57–L60.

Ćuk, M., Burns, J.A., 2005. Effects of thermal radiation on the dynamics of binary NEAs. Icarus 176, 418–431.

Ćuk, M., Nesvorný, D., 2010. Orbital evolution of small binary asteroids. Icarus 207, 732–743.

DeMeo, F.E., Binzel, R.P., Slivan, S.M., Bus, S.J., 2009. An extension of the Bus asteroid taxonomy into the near-infrared. Icarus 202, 160–180.

Ďurech, J., Kaasalainen, M., 2003. Photometric signatures of highly nonconvex and binary asteroids. Astron. Astrophys. 404, 709–714.

Gaskell, R. et al., 2006. Landmark navigation studies and target characterization in the Hayabusa encounter with Itokawa. AIAA paper 2006-6660. AAS/AIAA Astrodynamics Specialists Conference, Keystone, CO.

Higgins, D. et al., 2006. Asteroid lightcurve analysis at Hunters Hill Observatory and collaborating stations – Autumn/winter 2005. Minor Planet. Bull. 33, 8–10.

Hudson, S., 1993. Three-dimensional reconstruction of asteroids from radar observations. Rem. Sens. Rev. 8, 195–203.

Hudson, R.S., Ostro, S.J., 1994. Shape of Asteroid 4769 Castalia (1989 PB) from inversion of radar images. Science 263, 940–943.

Hudson, R.S., Ostro, S.J., 1999. Physical model of Asteroid 1620 Geographos from radar and optical data. Icarus 140, 369–378.

Hudson, R.S., Ostro, S.J., Harris, A.W., 1997. Constraints on spin state and Hapke parameters of Asteroid 4769 Castalia using lightcurves and a radar-derived shape model. Icarus 130, 165–176.

Hudson, R.S., Ostro, S.J., Scheeres, D.J., 2003. High-resolution model of Asteroid 4179 Toutatis. Icarus 161, 346–355.

Kaasalainen, M., Torppa, J., 2001. Optimization methods for asteroid lightcurve inversion. I. Shape determination. Icarus 153, 24–36.

Kaasalainen, M., Torppa, J., Muinonen, K., 2001. Optimization methods for asteroid lightcurve inversion. II. The complete inverse problem. Icarus 153, 37–51.

Kendall, M., Stuart, A., 1977. The Advanced Theory of Statistics, vol. 1: Distribution Theory, fourth ed. Macmillan, New York, pp. 397–402.

Krugly, Yu.N. et al., 2002. The near-Earth objects follow-up program. IV. CCD photometry in 1996–1999. Icarus 158, 294–304.

Krugly, Yu.N. et al., 2007. Kharkiv study of near-Earth asteroids. In: Milani, A., Valsecchi, G.B., Vokrouhlický, D. (Eds.), Near Earth Objects, our Celestial Neighbors: Opportunity and Risk. Proceedings of IAU Symposium No. 236. Cambridge University Press, Cambridge, pp. 385–390.

Magri, C. et al., 2007. Radar observations and a physical model of Asteroid 1580 Betulia. Icarus 186, 152–177.

McMahon, J., Scheeres, D.J., 2010. Detailed prediction for the BYORP effect on binary near-Earth Asteroid (66391) 1999 KW4 and implications for the binary population. Icarus 209, 494–509.

Ostro, S.J. et al., 2000. Radar observations of Asteroid 216 Kleopatra. Science 288, 836–839.

Ostro, S.J. et al., 2002. Asteroid radar astronomy. In: Bottke, W.F., Cellino, A., Paolicchi, P., Binzel, R.P. (Eds.), Asteroids III. Univ. of Arizona Press, Tucson, pp. 151–168.

Ostro, S.J. et al., 2004. Radar observations of Asteroid 25143 Itokawa (1998 SF36). Meteorit. Planet. Sci. 39, 407–424.

Ostro, S.J. et al., 2006. Radar imaging of binary near-Earth Asteroid (66391) 1999 KW4. Science 314, 1276–1280.

Ostro, S.J. et al., 2010. Radar imaging of Asteroid 7 Iris. Icarus 207, 285–294.

Pravec, P., Harris, A.W., 2007. Binary asteroid population. 1. Angular momentum content. Icarus 190, 250–259.

Rayner, J.T. et al., 2003. SpeX: A medium-resolution 0.8–5.5 micron spectrograph and imager for the NASA Infrared Telescope Facility. Publ. Astron. Soc. Pacific 115, 362–382.

Rubincam, D.P., 2000. Radiative spin-up and spin-down of small asteroids. Icarus 148, 2–11.

Scheeres, D.J., 2007a. The dynamical evolution of uniformly rotating asteroids subject to YORP. Icarus 188, 430–450.

Scheeres, D.J., 2007b. Rotational fission of contact binary asteroids. Icarus 189, 370–385.

Scheeres, D.J., 2009. Stability of the planar full 2-body problem. Celest. Mech. Dynam. Astron. 104, 103–128.

Scheeres, D.J., Ostro, S.J., Hudson, R.S., Werner, R.A., 1996. Orbits close to Asteroid 4769 Castalia. Icarus 121, 67–87.

Scheeres, D.J., Abe, M., Yoshikawa, M., Nakamura, R., Gaskell, R.W., Abell, P.A., 2007. The effect of YORP on Itokawa. Icarus 188, 425–429.

Scoles, S., Magri, C., Howell, E., Nolan, M., 2005. Physical modeling of near-Earth Asteroids 2005EU2 and 2002HK12. Bull. Am. Astron. Soc. 37, 642.

Shepard, M.K. et al., 2010. A radar survey of M- and X-class asteroids. II. Summary and synthesis. Icarus 208, 221–237.

Statler, T.S., 2009. Extreme sensitivity of the YORP effect to small-scale topography. Icarus 202, 502–513.

Taylor, P.A., 2009a. Preferential production of contact binary asteroids with components of similar mass via angular momentum loss. Bull. Am. Astron. Soc. 41, 905.

Taylor, P.A., 2009b. Tidal Interactions in Binary Asteroid Systems. Ph.D. Thesis, Cornell Univ., Ithaca, NY.